Fermi National Accelerator Laboratory

FN-561

Parton Distributions from Deep Inelastic Scattering *

H. E. Montgomery
Fermi National Accelerator Laboratory
P.O. Box 500
Batavia, Illinois 60510

August 1990

* Set of four talks presented in the Fermilab Academic Lecture Series, Batavia, Illinois, March 1989.

Operated by Universities Research Association Inc. under contract with the United States Department of Energy

Parton Distributions from Deep Inelastic Scattering *

H. E. Montgomery

Fermi National Accelerator Laboratory

P.O. Box 500
Batavia
Il 60510
USA

August 1990

Abstract

The primary source of information on the distributions of partons within the nucleon, is data on deep inelastic scattering of leptons on nucleons. The description of deep inelastic scattering is developed through the quark parton model including quantum chromodynamic corrections. The extraction of the quark and gluon momentum fraction distributions is illustrated using contemporary data. The extension to the case when the leptons and target are both polarized is presented and the recent data in this area are discussed. Finally, the differences observed in the data when the nucleons are embedded in nuclei are briefly discussed.

This report is a rather belated written version of a set of four talks presented in the Fermilab Academic Lecture Series in March 1989. The figures are largely copies of the transparencies used during the talks with little effort to clean them up.

*Work supported by the US Department of Energy

Contents

1 Lecture I

1.1 Introduction

These Lectures were given at Fermilab in the Spring of 1989. They were intended for an audience of graduate students in experimental high energy physics. The first two Lectures draw heavily on a previous set of Lectures given at the Arctic Summer School [1] some 8 years earlier. Overall, heavy reliance is made on a few contemporary graduate text books and review articles, these are listed as a bibliography. Except where tables are lifted verbatim from these sources, I do not make explicit reference to them. It should also be remarked that this is not a critical review of the present state of the subject. I used data plots which were conveniently available and although I have not deliberately used bad data, the reader should feel it incumbent on himself or herself to go directly to the sources before drawing weighty conclusions.

Considerable insight into the processes under study can be gleaned from considering the kinematics of the scattering of a simple electromagnetic particle from a target. This process is depicted in Fig. 1, in which an electron of energy E, momentum k is shown scattering through the exchange of a single photon from a target of mass M_t, 4-momentum P. If the scattering angle is θ and the final electron momentum k', then the scattering process can be described in terms of two Lorentz scalars $Q^2 = 4|\underline{k}||\underline{k}'|\sin^2\frac{\theta}{2}$ and $\nu = E - E'$. In the special case of elastic scattering, where the target remains intact then, if the target is initially at rest, the condition $Q^2 = 2M_t\nu$ obtains.

If we consider the scattering from some unspecified constituent of the target, also at rest, with mass M_c, then analogously, the condition $Q^2 = 2M_c\nu$ obtains. These two conditions are depicted on the kinematic plane, for the process, in Fig. 2.

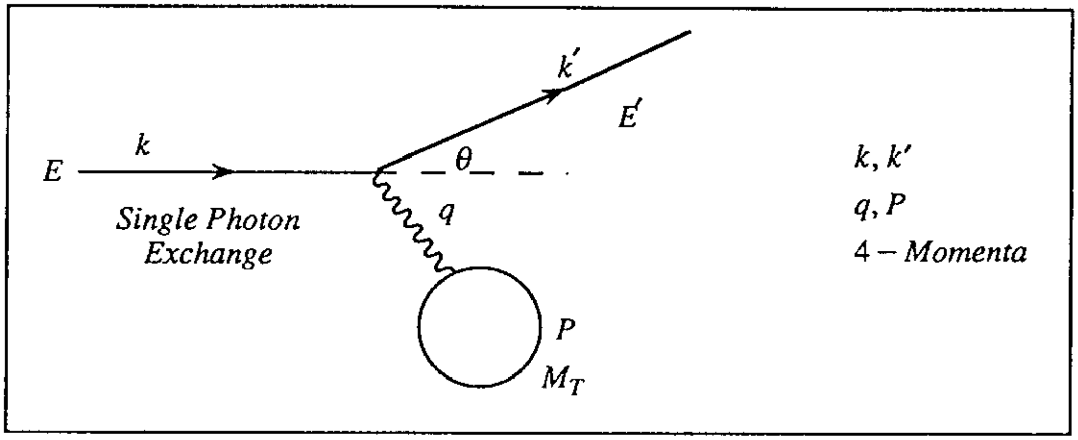

Figure 1: Single Photon Exchange Diagram for charged Lepton Scattering.

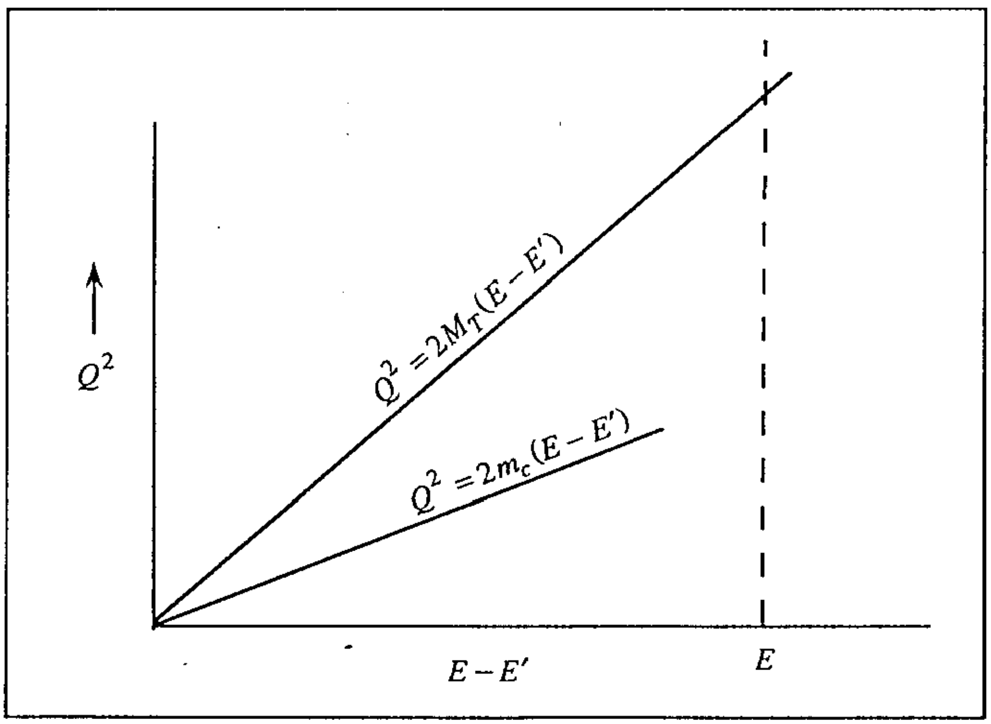

Figure 2: Kinematic Plane for Lepton Scattering.

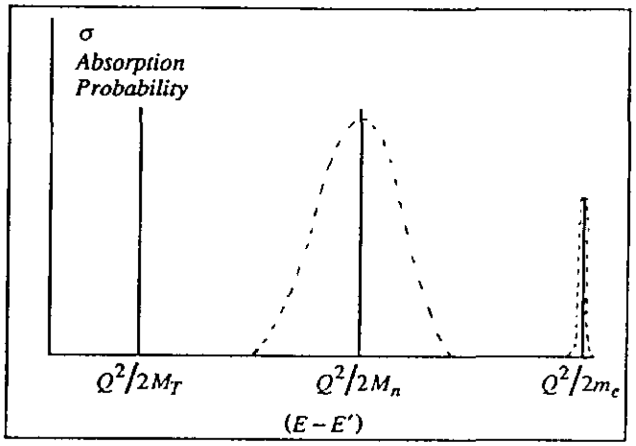

Figure 3: Notional Absorption Cross-section.

If we consider the realistic case of scattering from an atomic nucleus then the absorption cross-section will appear as shown in Fig. 3. Note that we also show the position of the line corresponding to scattering from the atomic electrons. This is also a process which is observed, even in the highest energy muon scattering experiments, and indeed forms an important background to the processes one wishes to study.

Note that the way we have labelled the axis and the foregoing discussion of the kinematics suggests that it will be useful to define the variable $x = Q^2/2M\nu$.

Let us now consider the Q^2 dependence of the process. We must remember that the photon couples to the charge of the target and that we may consider that $\sqrt{Q^2} \sim \text{Distance}^{-1}$. If the scattering is from a point source, or a pointlike distribution of charge, then the situation depicted in Fig. 4 obtains, there is no Q^2 dependence since the probe always sees ALL of the charge. If on the other hand the scattering is from an extended source, we have the situation sketched in Fig. 5, and there is a fall off of the cross-section as Q^2 is increased and the probe penetrates into the charge distribution.

The classic data shown in Figs. 6 and 7 is copied from the Annual Review article of Friedman and Kendall [2]. We observe in Fig. 6, the Elastic peak followed by the successive nucleon resonances as W is increased, and eventually a featureless continuum region appears. Data at fixed scattering angle and varying Q^2 are shown in Fig. 7. The resonances seem to disappear with increasing Q^2 whereas the continuum does not.

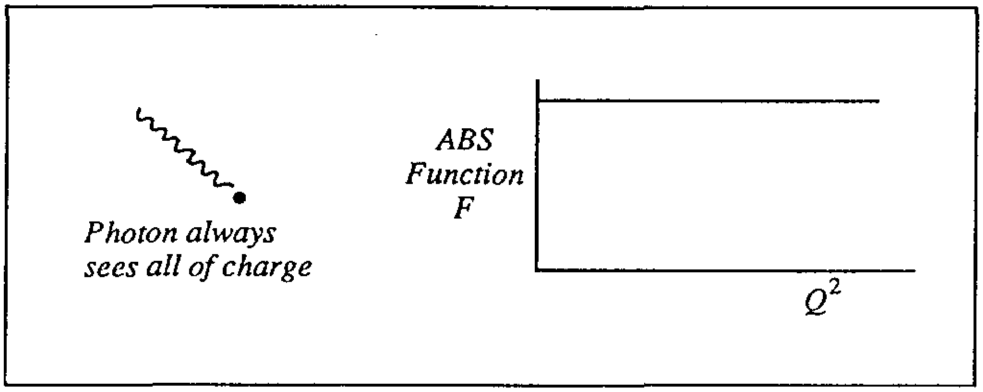

Figure 4: Scattering from Pointlike Charge.

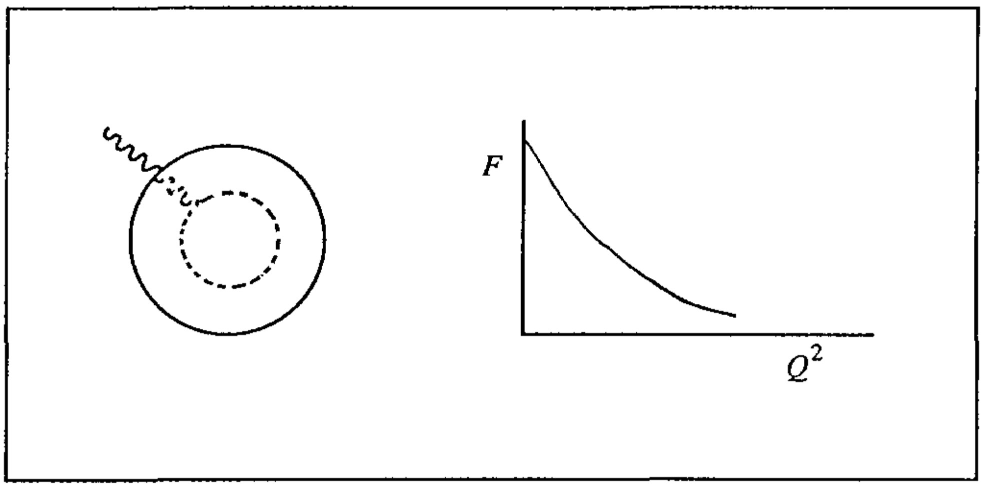

Figure 5: Scattering from Extended Charge Distribution.

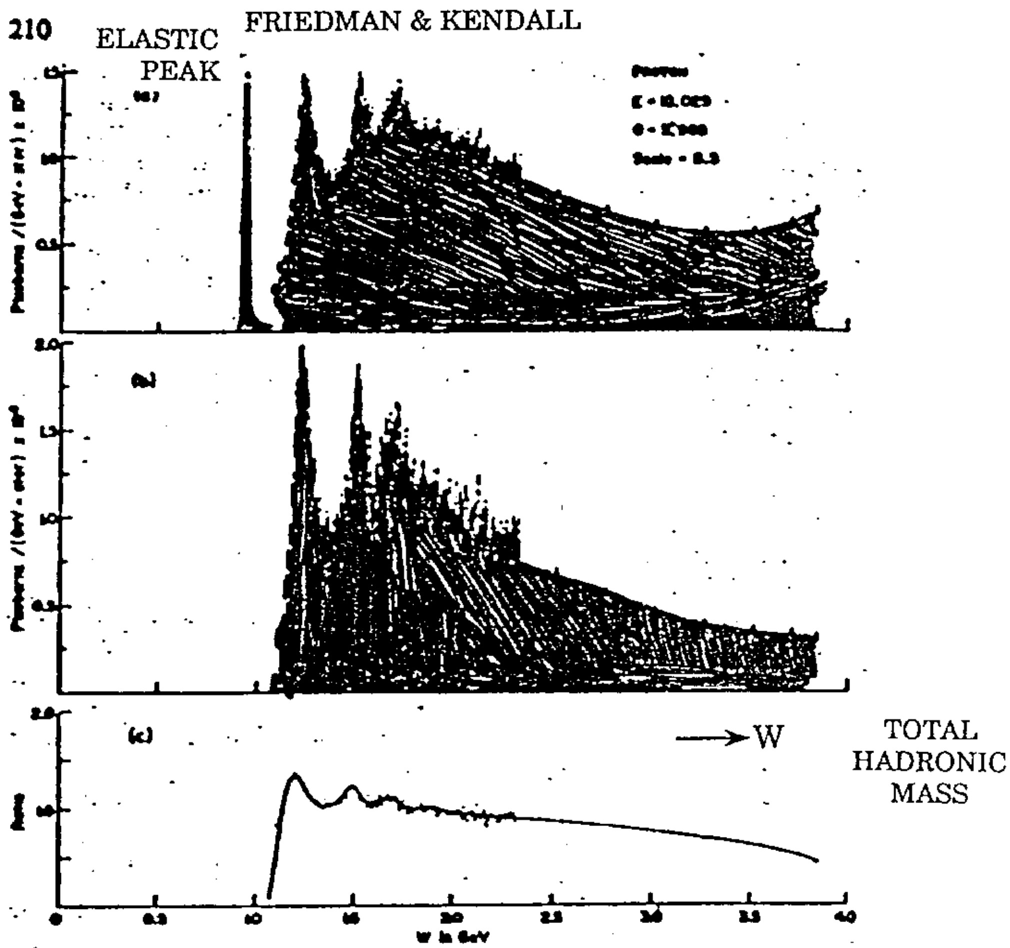

Spectra of 10 GeV electrons scattered from hydrogen at 6°, as a function of the final hadronic-state energy W. Figure (a) shows the spectrum before radiative corrections. The elastic peak has been reduced in scale by a factor of 8.5. The computed radiative tail from the elastic peak is shown. Figure (b) shows the same spectrum with the elastic peak's radiative tail subtracted and inelastic radiative corrections applied. Figure (c) shows the ratio of the inelastic spectrum before, to the spectrum after, radiative corrections.

Figure 6: Electron Scattering Data at 10 deg.

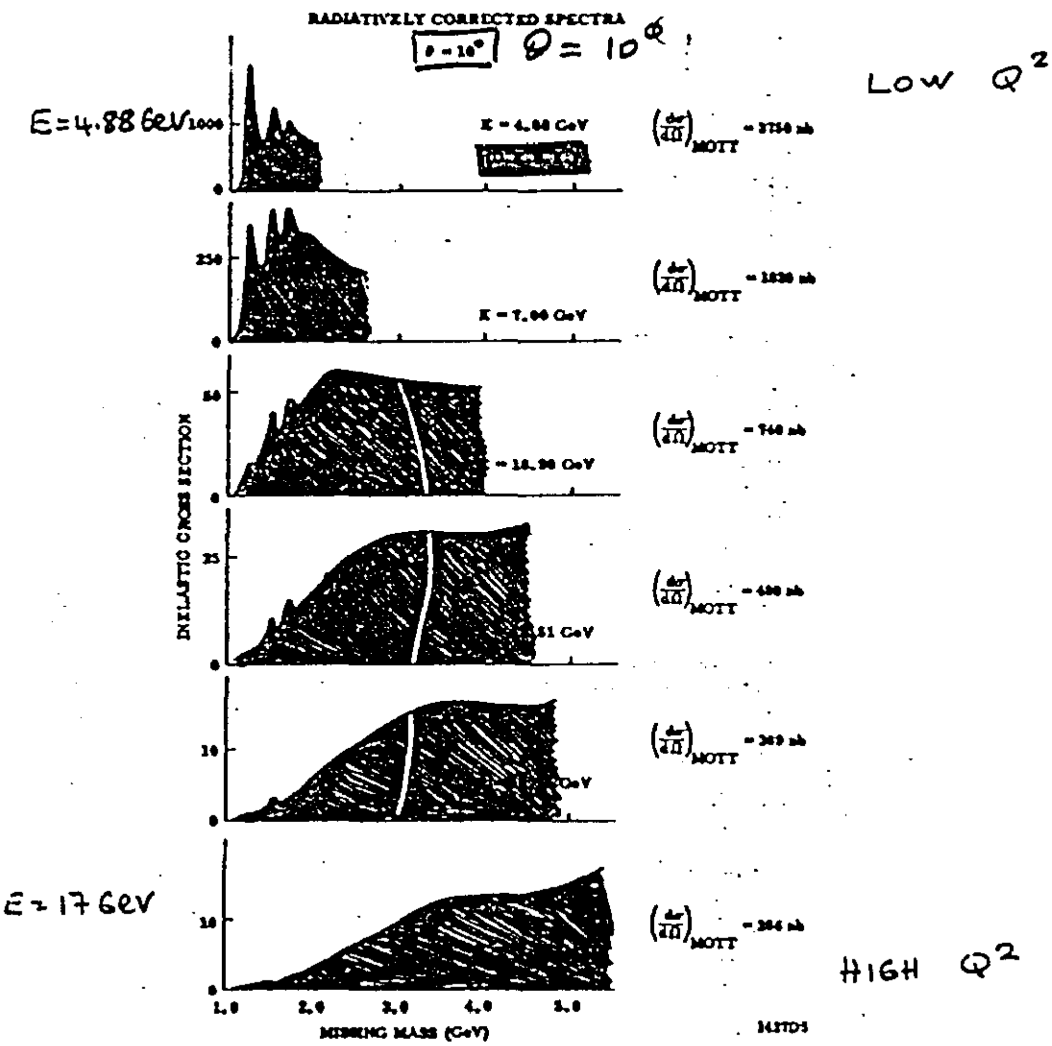

Visual fits to spectra showing the scattering of electrons from hydrogen at 10° for primary energies, E, from 4.88 GeV to 17.65 GeV. The elastic peaks have been subtracted and radiative corrections applied. The cross sections are expressed in nanobarns per GeV per steradian. The spectrum E-4.88 GeV was taken at DESY, Bartel W. *et al.* 1968. *Phys. Lett.* B 28:146.

Figure 7: Electron Scattering data at Fixed Angle, Different Q^2.

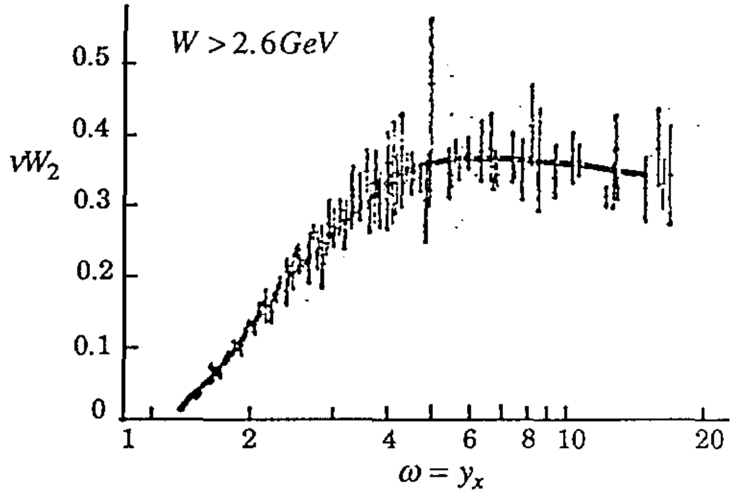

$2MW_1$ and νW_1 for the proton as functions of ω for W>2.6 GeV.
$q^2 > 1(GeV/c)^2$, and using R=0.18, Data from (8).

Figure 8: Electron Scattering Data as a Function of $1/x$.

These cross-section data may be considered to be

$$\sigma \sim QED{\cdot}Kinematics{\cdot}F(\nu, Q^2).$$

If the function F is extracted from the data for all angles and energies and is plotted as a function of the variable x introduced above, then we find, Fig. 8, that all the data appear to lie on a single universal curve. There is little or no residual Q^2 dependence.

Contact with a more rigorous theoretical treatment will follow later but we are tempted from these rather straightforward considerations to postulate:

1. *The scattering is from some constituents within the nucleon.*
2. *These objects are hard, pointlike.*

We can call these objects Partons and then ask the questions:

- *Are these quarks ?*

- *Are these interacting quarks?*
- *Are the interactions between the partons associated with Quantum Chromodynamics?*

The last 20 years have, so far, been spent investigating this avenue of thought. Here we devote a mere four Lectures to the subject, nevertheless, we will be helped by a considerable dose of hindsight.

1.2 Kinematics and Cross-sections

The basic process which we wish to consider was already introduced in Fig. 1, and the definitions of some kinematic quantities have already been given. On the other hand, to be tidy, I collect most of them here.

$$Q^2 = -q^2 = -(k-k')^2 = 4|\underline{k}||\underline{k}'|\sin^2\theta/2 \tag{1}$$

$$\nu = (p.q)/M = E - E' \tag{2}$$

$$y = \nu/E = (E-E')/E \tag{3}$$

$$x_{Bj} = Q^2/2M\nu = x \tag{4}$$

$$W^2 = 2M\nu - Q^2 \sim Q^2(1/x_{Bj} - 1). \tag{5}$$

We will pick these definitions up as needed later. Note that the subscript Bj recognizes that this scaling behavior was predicted by Bjorken [3].

In order to derive the cross-section for the process shown in Fig. 1, it is easiest to start from the simpler situation where the target particle is also a charged lepton. An example process would be electron muon elastic scattering, shown in Fig. 9.

$$e + \mu \to e + \mu. \tag{6}$$

Let the momenta and energies be generally defined

$$\underline{k} + \underline{p} \to \underline{k}' + \underline{p}', \tag{7}$$

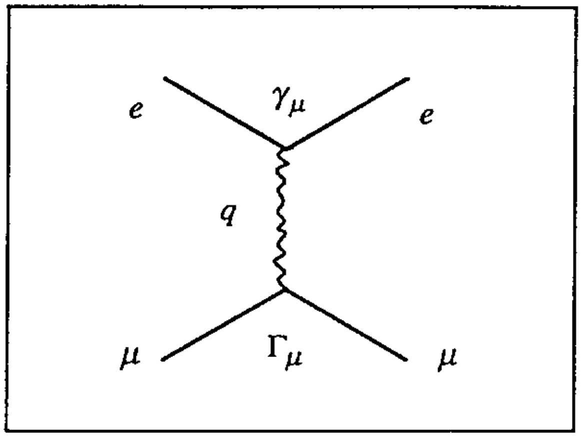

Figure 9: Elastic Electron Muon Scattering.

$$E + E_2 \rightarrow E' + E_4. \tag{8}$$

The equation for the cross-section is given by

$$d\sigma = \frac{1}{\mid v_1 - v_2 \mid} \frac{1}{2E_1E_2} \mid M \mid^2 \frac{d^3k'}{2E'} \frac{d^3p'}{2E_4} (2\pi)^4 \delta^4(k + p + k' + p'). \tag{9}$$

The physics is all contained in the $\mid M \mid^2$, matrix element term. It is the product of the vertex functions and the propagator for the exchanged boson.

$$\mid M \mid^2 = \frac{1}{4} \sum_{s_1 s_2 s_3 s_4} \mid \overline{u}(k')\gamma_\mu u(k) \frac{e^2}{q^2} \overline{u}(p')\Gamma\mu u(p) \mid^2, \tag{10}$$

$$\mid M \mid^2 = \frac{e^4}{q^4} \mathcal{L}_{\mu\nu} \mathcal{W}^{\mu\nu}. \tag{11}$$

The electron tensor is given by

$$\mathcal{L}_{\mu\nu} = \frac{1}{2} Tr(\not{k}' + m)\gamma_\mu(\not{k} + m)\gamma_\nu, \tag{12}$$

$$\mathcal{L}_{\mu\nu} = 2[k'_\mu k_\nu + k_\mu k'_\nu + g_{\mu\nu}(\underline{k}.\underline{k}' - m^2], \tag{13}$$

and the muon tensor by

$$\mathcal{W}_{\mu\nu} = \frac{1}{2}Tr(\not{k}' + M)\Gamma_\mu(\not{k} + M)\Gamma_\nu. \tag{14}$$

By making different choices for the Γ_μ we can choose the interaction we wish to consider. If we take the case that the target is a simple muon of mass M, then we have $\Gamma_\mu = \gamma_\mu$ and

$$\mathcal{L}_{\mu\nu}\mathcal{W}^{\mu\nu} = 8[\underline{k}'.\underline{p}\underline{k}.\underline{p} + \underline{p}.\underline{k}'\underline{k}.\underline{p}' - m^2\underline{p}.\underline{p}' + M^2\underline{k}.\underline{k}' + 2m^2M^2]. \tag{15}$$

If we now work in the laboratory frame, $p = (M, 0)$, $k = (E, \underline{k})$, $k' = (E', \underline{k})$ and $q^2 = (k - k')^2$, neglecting higher order terms in the masses we find

$$\mathcal{L}_{\mu\nu}\mathcal{W}^{\mu\nu} = 8[2M^2EE' + \frac{q^2M(E - E')}{2} + \frac{M^2q^2}{2}], \tag{16}$$

and

$$\mathcal{L}_{\mu\nu}\mathcal{W}^{\mu\nu} = 16M^2EE'[\cos^2(\theta/2)\mathcal{A} - \frac{q^2}{2M^2}\sin^2(\theta/2)\mathcal{B}]. \tag{17}$$

Finally, we obtain for the cross-section

$$\frac{d^2\sigma}{d\Omega dE'} = \frac{4\pi\alpha^2(E')^2}{Q^4}[\cos^2(\theta/2)\mathcal{A} + \frac{Q^2}{2M^2}\sin^2(\theta/2)\mathcal{B}]\delta(2M\nu - Q^2). \tag{18}$$

In both of the above equations, $\mathcal{A}$ and $\mathcal{B}$ are equal to unity. Later as we generalize this equation to more complicated processes, we will see that it is the $\mathcal{A}$ and $\mathcal{B}$ which are modified. They carry the information concerning the structure of the scattering particles. In particular, if we modify the Γ_μ to describe a proton, then the $\mathcal{A}$ and $\mathcal{B}$ become $\mathcal{A}(Q^2)$ and $\mathcal{B}(Q^2)$ and can be identified with the elastic form factors of the proton. For the case of inelastic scattering from a proton target we get a further modification.

$$\frac{d^2\sigma}{d\Omega dE'} = \frac{4\pi\alpha^2(E')^2}{Q^4}[\cos^2(\theta/2)\mathcal{A}(\nu, Q^2) + \frac{Q^2}{2M^2}\sin^2(\theta/2)\mathcal{B}(\nu, Q^2)]. \tag{19}$$

The δ function corresponding to the elastic scattering condition disappears and the $\mathcal{A}$ and $\mathcal{B}$ are now functions of two variables, here we take those variables to be Q^2 and ν but any pair will do. Alternatively, equivalent expressions of the inelastic cross-section for charged lepton (e,μ) scattering are:

$$\frac{d^2\sigma}{d\Omega dE'} = \frac{4\pi\alpha^2(E')^2}{Q^4}[\cos^2(\theta/2)\mathcal{W}_2(\nu,Q^2) + 2\sin^2(\theta/2)\mathcal{W}_1(\nu,Q^2)], \tag{20}$$

and

$$\frac{d^2\sigma}{d\Omega dE'} = \Gamma[\sigma_t + \epsilon\sigma_l]. \tag{21}$$

$\frac{\sigma_l}{\sigma_t} = R$ is the ratio between the absorption cross-sections for longitudinally and transversely polarized photons. In the real photon limit, $Q^2 = 0$, the photon has only transverse components and hence only contributions from σ_t. Finally, the most usual present day form defines two structure functions $\mathcal{F}_1$ and $\mathcal{F}_2$.

$$\frac{d^2\sigma}{dxdy} = \frac{4\pi\alpha^2 ME}{Q^4}[y^2x\mathcal{F}_1(x,Q^2) + (1-y-\frac{Mxy}{2E})\mathcal{F}_2(x,Q^2)]. \tag{22}$$

Since there is some evidence that for a large kinematic range, R is relatively small, it is also usual to mix notations such that F_2 dominates both in actuality and in notation,

$$\frac{d^2\sigma}{dxdQ^2} = \frac{4\pi\alpha^2}{Q^4x}[(1-y) + \frac{y^2}{2(1+R)} + \frac{Q^2}{2E^2}(\frac{1}{(1+R)} - \frac{1}{2})]\mathcal{F}_2(x,Q^2). \tag{23}$$

For neutrino and anti-neutrino scattering there are analogous expressions,

$$\frac{d^2\sigma}{dxdy}^{\nu} = \frac{G^2ME}{\pi}[y^2x\mathcal{F}_1(x,Q^2)+(1-y-\frac{Mxy}{2E})\mathcal{F}_2(x,Q^2)+y(1-\frac{y}{2})x\mathcal{F}_3(x,Q^2)] \tag{24}$$

$$\frac{d^2\sigma}{dxdy}^{\overline{\nu}} = \frac{G^2ME}{\pi}[y^2x\mathcal{F}_1(x,Q^2)+(1-y-\frac{Mxy}{2E})\mathcal{F}_2(x,Q^2)-y(1-\frac{y}{2})x\mathcal{F}_3(x,Q^2)] \tag{25}$$

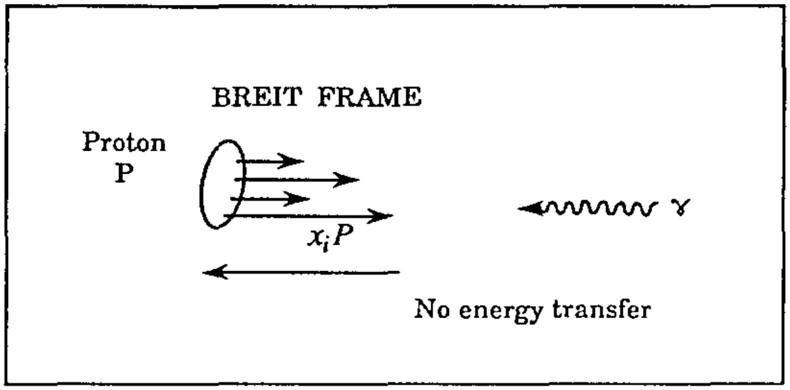

Figure 10: Breit Frame view of Photon Absorption by constituent.

1.3 Contact with the Parton Model

If we consider how a virtual photon can be absorbed by a constituent of the proton, we have the situation depicted in Fig. 10, in which we choose to work in the frame in which the scattering process simply reverses the parton 3-momentum and there is no energy transfer. Let the parton momentum be $x_i P$ where P is the proton momentum. If β and γ are the appropriate Lorentz factors for transformation from the lab to this Breit frame, then for the photon energy we have,

$$0 = \gamma(\nu - q\beta), \tag{26}$$

for the proton momentum,

$$P = \gamma\beta M, \tag{27}$$

and for the parton momentum,

$$2x_i P = \gamma(q - \beta M). \tag{28}$$

This can be rearranged to yield,

$$x_i = \frac{Q^2}{2M\nu}, \tag{29}$$

identifying x_{Bj} with the momentum fraction of the proton carried by the parton.

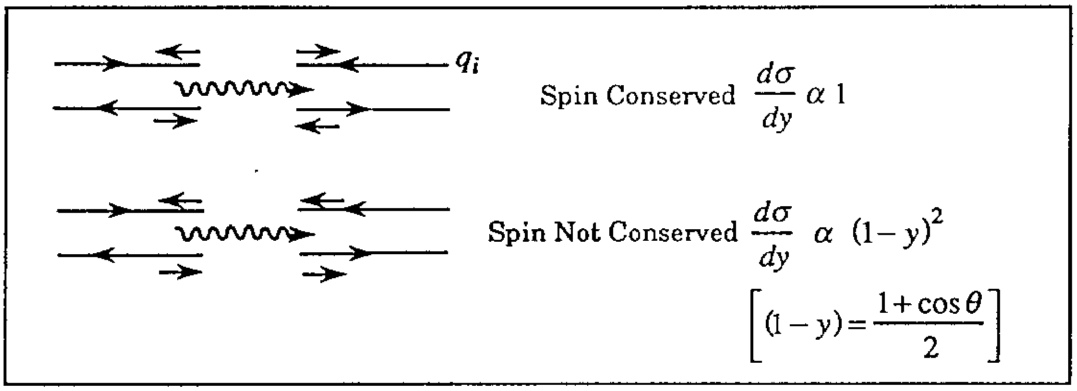

Figure 11: Spin Transfer in the Breit Frame.

The basic component of the coupling between two leptons, electron and parton, is the vector γ_μ, this may be decomposed into left and right handed components

$$\gamma_\mu = \frac{1}{2}(\gamma_\mu(1-\gamma_5) + \gamma_\mu(1+\gamma_5)). \tag{30}$$

The cross-section for a single quark also displays the results of this decomposition,

$$\frac{d\sigma}{dy} \simeq \frac{1}{2}\left(1 + (1-y)^2\right), \tag{31}$$

$$\frac{d^2\sigma}{dy} = \frac{4\pi\alpha^2 ME}{Q^4} {q_i}^2 \frac{1}{2}[1 + (1-y)^2]. \tag{32}$$

The term in $(1-y)^2$ arises because, as indicated in Fig. 11, the backward scattering between two leptons with initially aligned spins is suppressed.

If we now construct the cross-section for scattering for an ensemble of partons labelled i with charge q_i and momentum fraction x which is distributed according to some function $f_i(x)$

$$\frac{d^2\sigma}{dxdy} = \frac{4\pi\alpha^2 ME}{Q^4}(\Sigma {q_i}^2 x f_i(x))\frac{1}{2}[1 + (1-y)^2], \tag{33}$$

which yields

$$\frac{d^2\sigma}{dxdy} = \frac{4\pi\alpha^2 ME}{Q^4}(\Sigma q_i{}^2 x f_i(x))[\frac{y^2}{2} + (1-y)]. \tag{34}$$

Comparison with one of the earlier stated forms of the cross-section leads to the identification:

$$2xF_1 \longleftrightarrow \sum q_i^2 x f(x), \tag{35}$$

which is the basic quark parton model relationship.

1.4 Experiments

The main purpose of these Lectures is to progress from the basic theoretical treatment of the subject to an appreciation of what we actually have understood. This process clearly will involve data. As mentioned in the introduction there will not be an exhaustive treatment of all the data. However, it is important that we have some appreciation of the limitations of the different experiments, especially if we wish to make comparisons between the different results.

The standard of deep inelastic scattering data is now such that for many aspects the dominant errors are not statistical, in many bins cross-sections are determined with 1% statistical uncertainty. The errors which affect the phenomenology most are the systematic errors. Many of these are basic systematic uncertainties related to the different experimental methods. However, there are also potential differences in results arising from variations in the way the data are treated before presentation for phenomenological analysis. I will not treat the latter here, however, a group of resolute persons [4] made an effort at Snowmass in 1988 to develop an appreciation of the diversity and to recommend particular remedies. Here we will satisfy ourselves with a very brief description of the different experiments in generic terms.

Experimentally, the cross-section is a function of three variables, the incident lepton energy E, the scattered lepton energy E', and the lepton scattering angle θ,

$$\frac{d\sigma}{dxdQ^2} = f(E, E', \theta), \tag{36}$$

or equivalent combinations. The target is assumed to be at rest, there is no argument for a hydrogen target but with nuclear targets there are issues related to the fermi motion of the nucleons.

Muon experiments [5, 6, 9] actually measure E, E' and θ directly. The large electronic neutrino experiments [7, 8] cannot measure the beam energy directly, so they measure E', θ, and the energy E_h of the final hadronic state using calorimetry.

There are several different types of neutrino beam, the type used in a major part of the structure function work is the Narrow Band beam. It is so called because when the extracted primary protons are targetted to produce a beam of secondary pions and kaons, the momentum of those mesons is restricted, hence, narrow band. The two meson types each produce neutrinos in their decay and the kaons, which are in the minority, produce higher energy neutrinos than the pions. In such a beam it is possible to determine the relative fractions of π and k using Cerenkov techniques. These measurements are combined with measurements of the production spectra and a determination of the number of incident protons to determine the flux of neutrinos. This is an involved process and is often supplemented by attempts to also measure the flux of muons produced in the same decays as produce the neutrinos. Because of the difficulties, typical quoted errors are often greater than 5%, although major effort to produce and use ancilliary methods [10] are yielding possibilities for the future.

The neutrino energy is even more difficult to obtain. With a narrow band beam there is a corelation, related to the decay kinematics, between the impact point of the neutrino on the detector and the energy of the neutrino. However, this is not of sufficiently good precision to be more than a check. The primary determination is by calorimetric measurement of the hadronic energy. A sketch of the Lab E Fermilab apparatus [8] is shown in Fig. 12, the calorimetric measurements are provided by the liquid scintillation counters which are distributed at 10cm intervals through the target.

The resolution of this measurement is typically $\frac{\sigma_E}{E} = \frac{0.8}{\sqrt{E}} + const$, and with care, the absolute scale can be fixed to better than 1%. That this is important is demonstrated in Fig. 13, where we plot the ratio between the true and measured $\mathcal{F}_2$ for a postulated small error in scale and linearity.

A sketch of the BCDMS muon scattering apparatus [6] is shown in Fig. 14. The incident energy of samples of incident beam particles, and all those

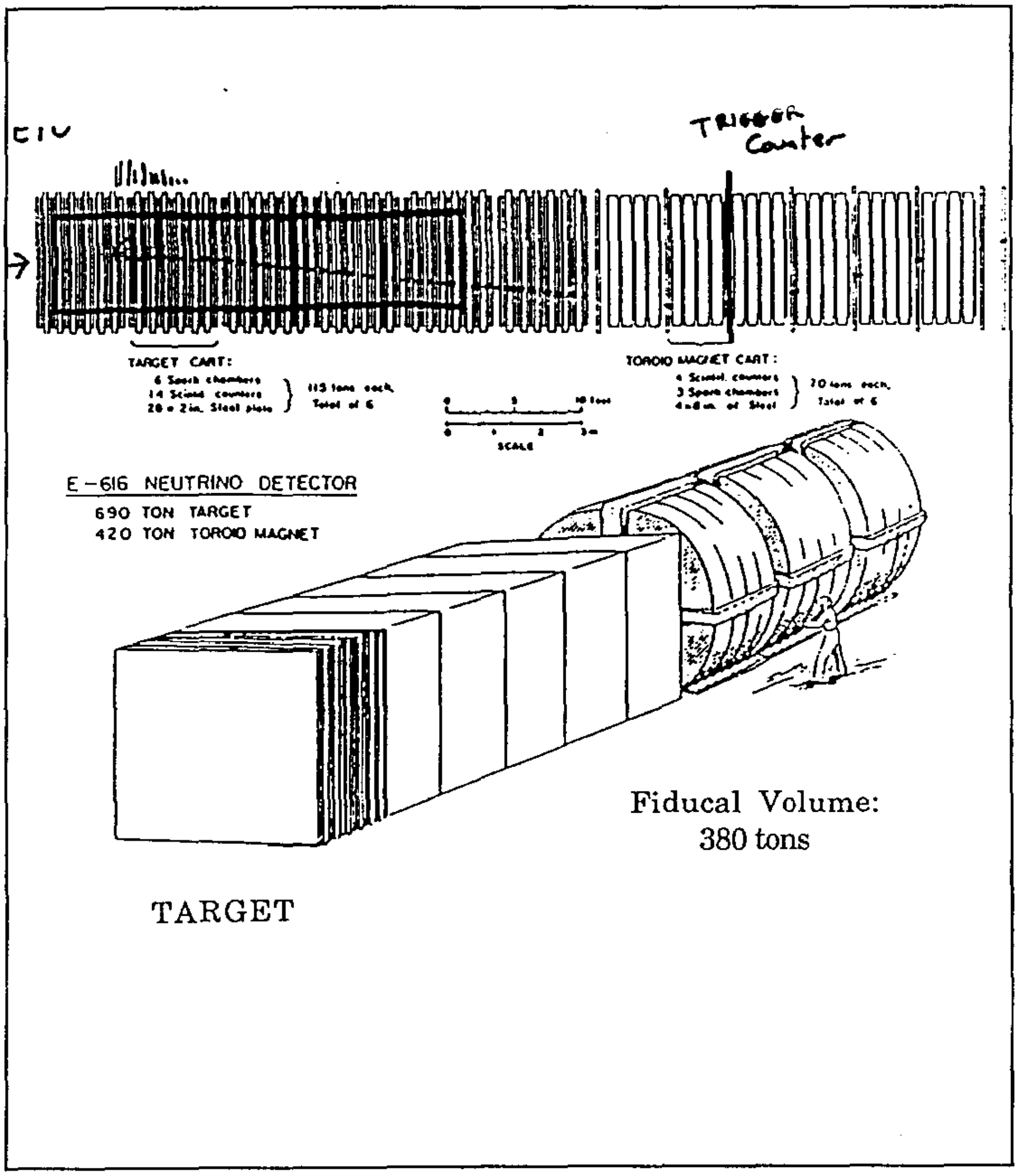

Figure 12: Sketch of CCFR, Lab E Neutrino Detector at Fermilab.

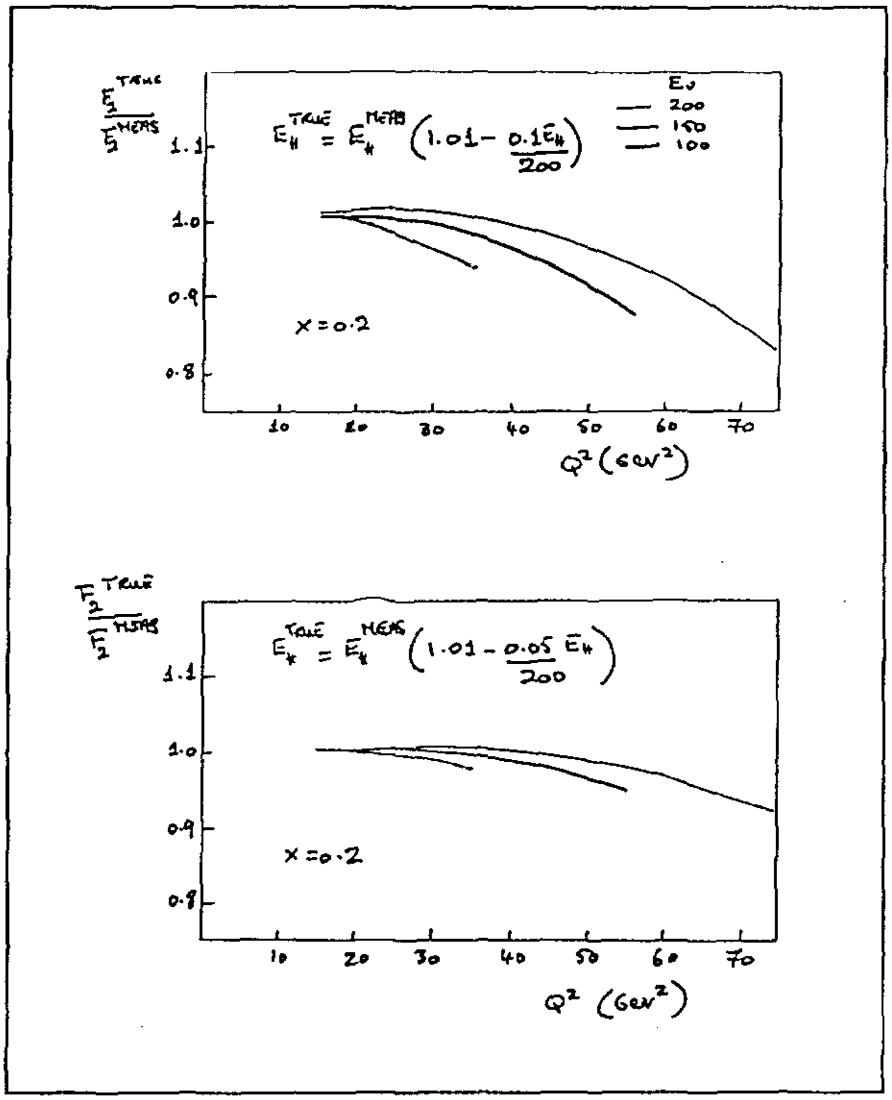

Figure 13: Effects on $\mathcal{F}_2$ of small errors in the calorimeter calibration in a neutrino experiment.

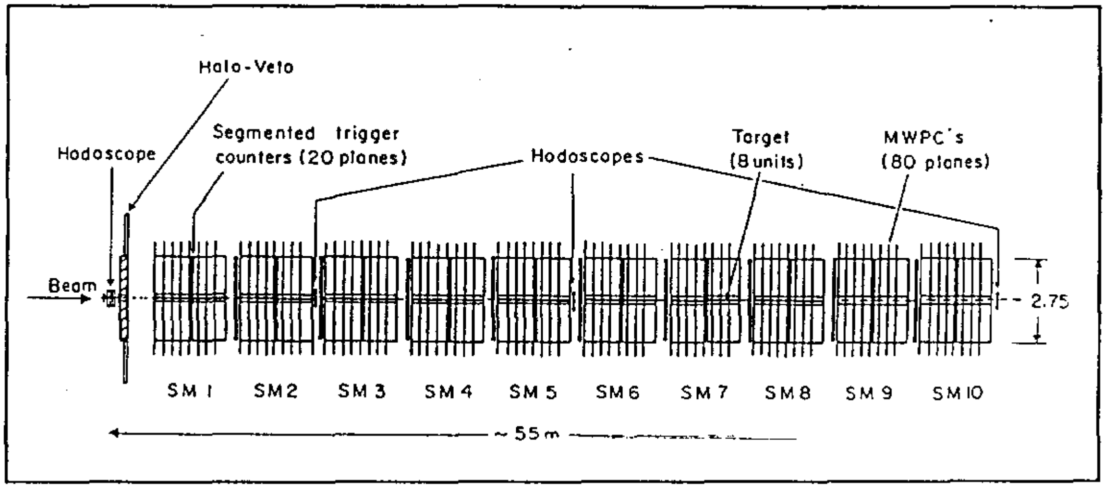

Figure 14: The BCDMS Apparatus.

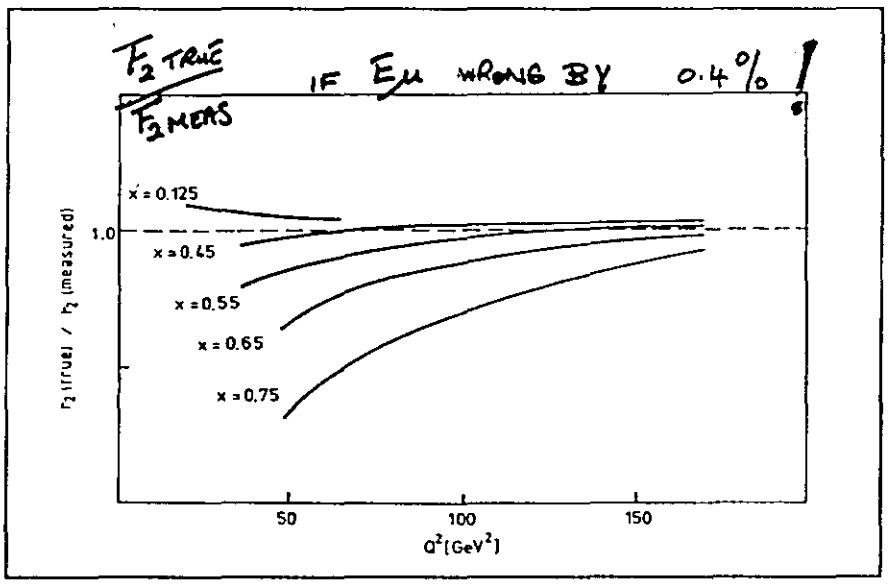

Figure 15: Effects on $\mathcal{F}_2$ of a small error in the calibration of the incident muon spectrometer in a muon scattering experiment.

which are used in the cross-section determination, are measured with a resolution of 0.3%. The absolute scale of this measurement is related to that of the muon spectrometer by displacing the beam such that muons are measured and compared on an event by event basis in each of the beam and scattered muon spectrometers. BCDMS, as seen in Fig. 14, used an iron toroid spectrometer and unusual efforts had to be made to determine the magnetic field in the iron. Their quoted error is $\frac{\Delta B}{B} = 0.15\%$, however, in recent attempts to envisage a better experiment [11, 12], an air core toroid has been deliberately chosen.

As a check on the momentum scale in their spectrometer EMC [5] have used the J/Ψ dimuon peak and obtained good agreement with the published value. This and other checks in all experiments give confidence at the level of 0.4%. On the other hand, the results of such a small error are demonstrated in Fig. 15. They are clearly not negligible.

I have tried, in this section, to give a feel for the kinds of systematic errors which the experimenter is fighting on a day to day basis. The residual errors in all experiments to date are of the order of 5% in normalization and there may also be systematic tilts as a function of one variable or another of the order of 10%. This is most forcefully brought home when one considers the checkered history of the neutrino total cross-section determinations [13, 14] and the current disagreements between the two highest luminosity muon scattering experiments [15].

2 Lecture II

2.1 Quark Parton Model: Motivation

In the previous Lecture we suggested that the variable x_{Bj} could be interpreted as the momentum fraction of the target nucleon carried by the parton participating in the scatter. In this Lecture we wish to start from this quark parton model (QPM) hypothesis, to develop some predictions and to make comparison with some representative data. The examples considered here will be comparatively straightforward. For a contemporary discussion of the state of the art in this field, the reader should consult the review article by Sloan, Smadja and Voss.

Our starting point is that within the QPM, assuming only spin $\frac{1}{2}$ partons,

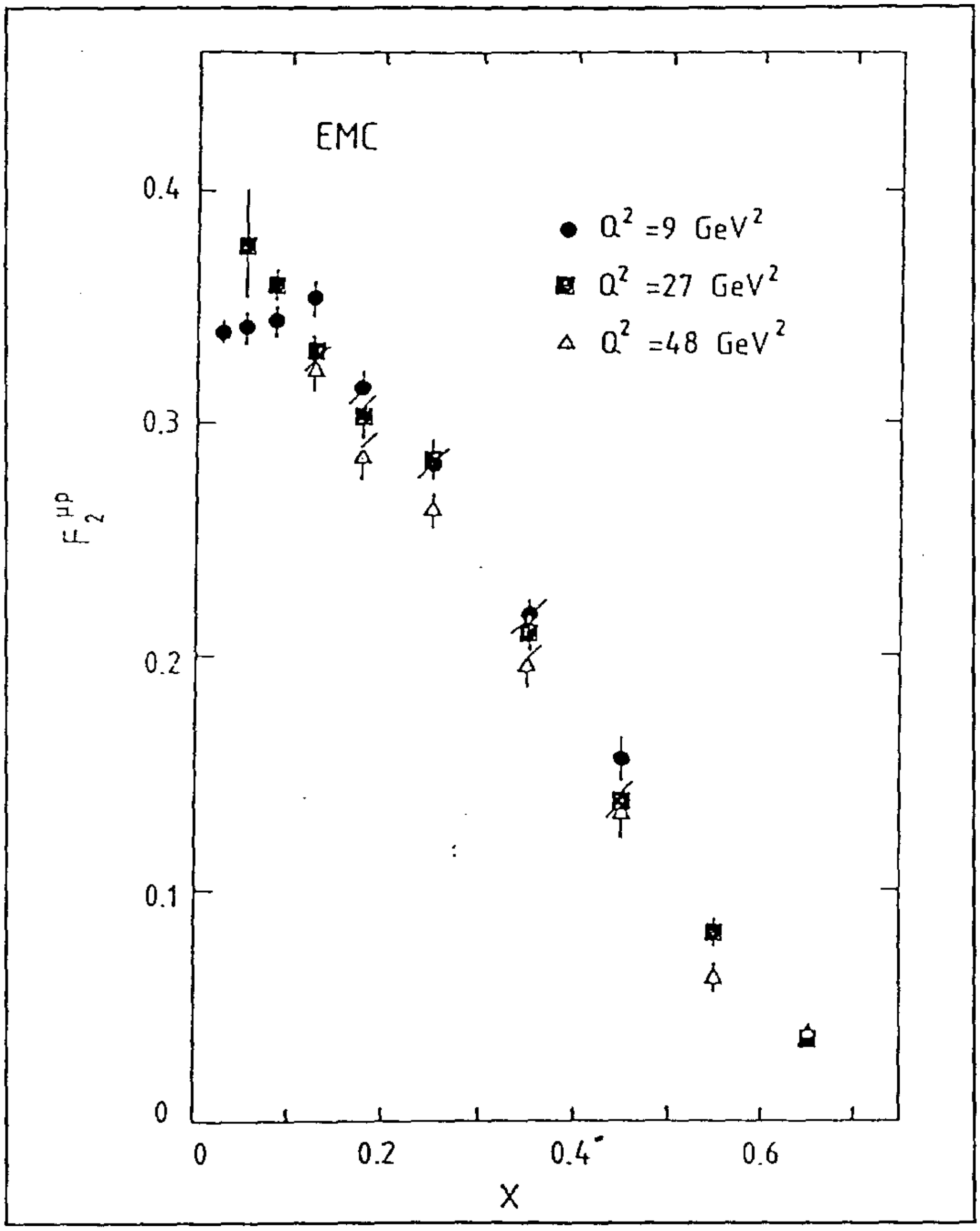

Figure 16: The Structure Function $\mathcal{F}_2$ at different values of Q^2.

$$2x\mathcal{F}_1 = \mathcal{F}_2 = \sum q_i^2 x f(x) \tag{37}$$

where q_i are the quark electromagnetic charges. Analogous expressions in which the electromagnetic couplings are replaced by the weak couplings are given for neutrino scattering by Fisk and Sciulli. The immediate consequence and indeed, as we have seen, one of the driving observations behind the model is that the structure functions are independent of Q^2. In Fig. 16, we see how over the range $9GeV^2 < Q^2 < 48GeV^2$ this is indeed true at the level of 10%.

Let us now consider the structure functions for a proton target more explicitly.

$$\mathcal{F}_2{}^{e,\mu p}(x) = \frac{4}{9}x[u^p(x) + \overline{u}^p(x)] + \frac{1}{9}x[d^p(x) + \overline{d}^p(x)] + \frac{1}{9}x[s^p(x) + \overline{s}^p(x)] \tag{38}$$

where $u^p(x)$ is the distribution of u quarks in the proton. If we now drop the superscript p for the proton case but apply isospin symmetry we have $u^n = d$ and $d^n = u$. The anti-quark distributions are taken to be independent of whether the target is proton or neutron and we find

$$\mathcal{F}_2^{e,\mu p}(x) = \frac{4}{9}x[u + \overline{u}] + \frac{1}{9}x[d + \overline{d}] + \frac{1}{9}x[s + \overline{s}] + \frac{4}{9}x[c + \overline{c}] \tag{39}$$

where for brevity, we have dropped reference to the fact that each of these entities is a function of x. For the neutron we obtain

$$\mathcal{F}_2^{e,\mu n}(x) = \frac{1}{9}x[u + \overline{u}] + \frac{4}{9}x[d + \overline{d}] + \frac{1}{9}x[s + \overline{s}] + \frac{4}{9}x[c + \overline{c}]. \tag{40}$$

If measurements are made from an isoscalar target, for instance, the Deuteron or, to some approximation, Iron, then the effective $\mathcal{F}_2$ per nucleon is

$$\mathcal{F}_2^{eN}(x) = \frac{\mathcal{F}_2^{ep}(x) + \mathcal{F}_2^{en}(x)}{2} \tag{41}$$

$$\mathcal{F}_2^{eN}(x) = \frac{5}{18}x[u + \overline{u} + d + \overline{d}] + \frac{1}{18}x[s + \overline{s}] + \frac{4}{18}x[c + \overline{c}]. \tag{42}$$

There are similar expressions for neutrino scattering. Before we start to work some examples we should note that there are some obvious QPM Sum Rules.

Nucleon Strangeness

$$\int_0^1 dx[s+\bar{s}] = 0 \tag{43}$$

Proton Charge

$$\int_0^1 dx[\frac{2}{3}(u-\bar{u}) - \frac{1}{3}(d-\bar{d})] = 1 \tag{44}$$

Neutron Charge

$$\int_0^1 dx \left[\frac{2}{3}(d-\bar{d}) - \frac{1}{3}(u-\bar{u})\right] = 0, \tag{45}$$

and consequently

$$\int_0^1 dx(u-\bar{u}) = 2, \tag{46}$$

and

$$\int_0^1 dx[(d-\bar{d})] = 1. \tag{47}$$

Finally, the Gross-Llewellyn Sum Rule counts quarks, see Eq. 52.

$$\int_0^1 \mathcal{F}_3^{\nu N} dx = q - \bar{q}. \tag{48}$$

2.2 Quark Parton Model: Some Examples

2.2.1 Proton, Neutron Difference and Ratio

From our expressions for the proton and neutron structure functions, we obtain

$$\mathcal{F}_2^{e,\mu p} - \mathcal{F}_2^{e,\mu n} = \frac{x}{3}[u-d]. \tag{49}$$

We should note that in this expression there is no reference to anti-quarks, the only components of the quark distributions are those contributing to the quantum numbers. These are often called the valence quarks. In the scattering of electrons from a nucleus, a bump is observed corresponding to the quasi-elastic scattering from the individual nucleons. The idea that

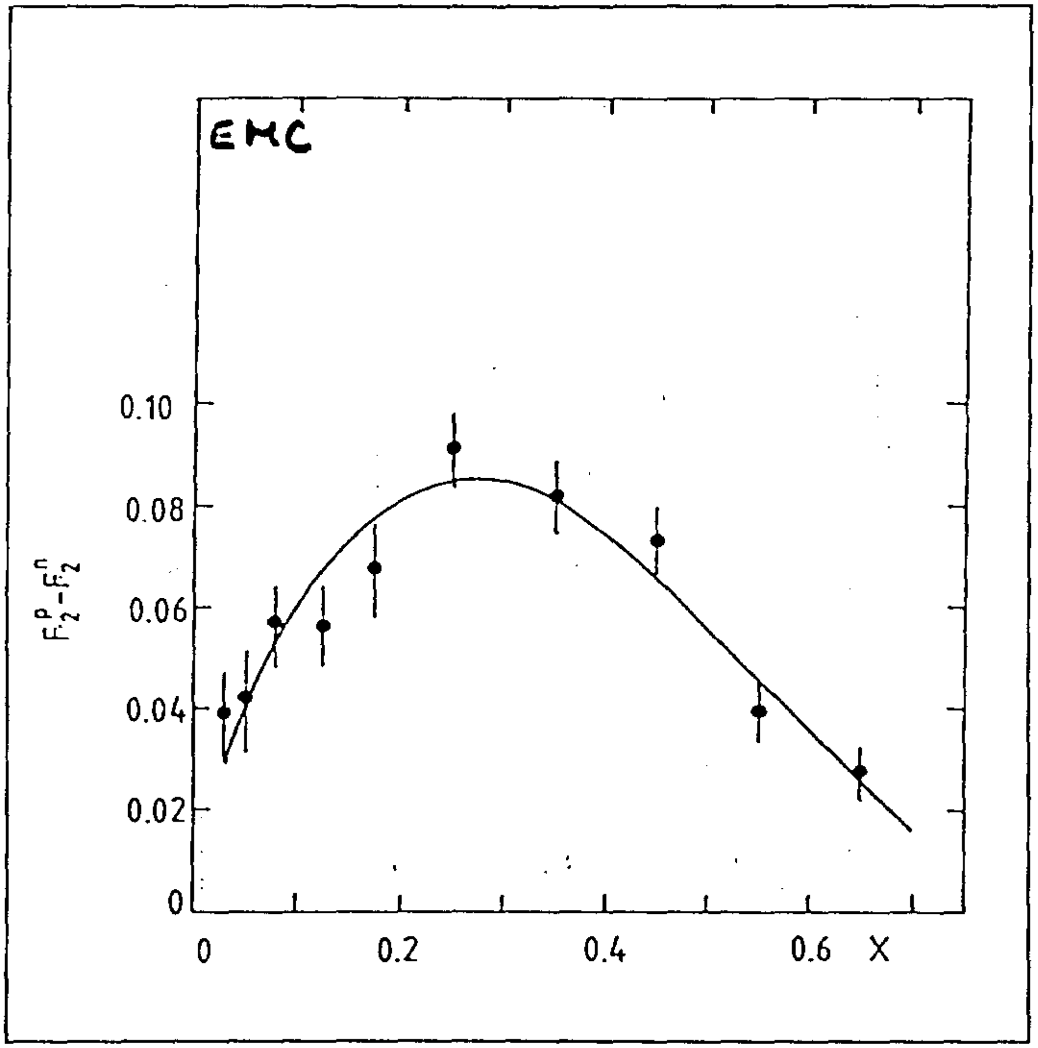

Figure 17: Proton Neutron Structure Function Difference.

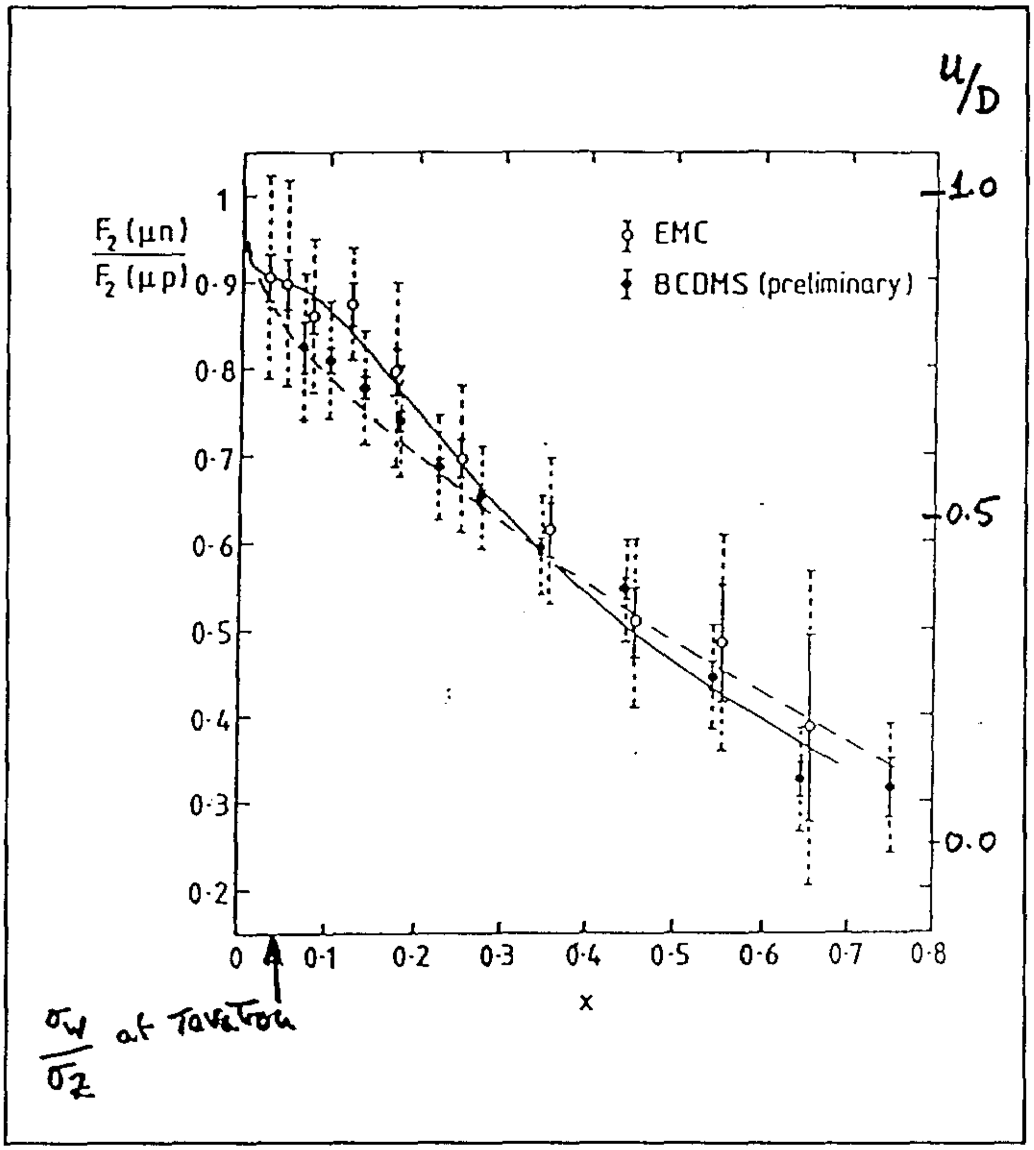

Figure 18: Neutron Proton Structure Function Ratio.

we might observe quasi-elastic scattering from constituents was introduced earlier and indeed in the data, see Fig. 17, there does indeed appear to be a broad peak at about $x = \frac{1}{3}$. There is a corresponding sum rule due to Gottfried which states

$$\int_0^1 \frac{1}{x}(\mathcal{F}_2^{\mu p} - \mathcal{F}_2^{\mu n})dx = \frac{1}{3}, \tag{50}$$

the data yield $0.24 \pm 0.02(stat) \pm 0.13(syst)$, where a lot of the error comes from the lack of data at low x. The ratio of structure functions is bounded $\frac{1}{4} < \frac{\mathcal{F}_2^{\mu n}}{\mathcal{F}_2^{\mu p}} < 4$ and the data, Fig. 18, approach the QPM limit at high x suggesting that the u quark distribution in the proton persists to higher x than the d quark distribution. The tendency to unity at low x is consistent with the disappearance of the valence quarks (Fig. 17) as $x \rightarrow 0$ and the dominance by the quark-antiquark sea, which is expected to be approximately symmetric between proton and neutron.

2.2.2 Separation of Quark and Anti-quark Distributions

We can see from Eqs. 24 and 25 that if we take the sum of the cross-sections for neutrinos and anti-neutrinos we can extract $\mathcal{F}_2^{\nu N}$ and if we take the difference we can obtain $\mathcal{F}_3^{\nu N}$. Now

$$\mathcal{F}_2^{\nu N} = x[u(x) + d(x) + \overline{u}(x) + \overline{d}(x) + ...], \tag{51}$$

$$x\mathcal{F}_3^{\nu N} = x[u(x) + d(x) - \overline{u}(x) - \overline{d}(x) + ...], \tag{52}$$

and we can construct

$$\mathcal{F}_2^{\nu N} + x\mathcal{F}_3^{\nu N} = x[u(x) + d(x) + ...] = q(x), \tag{53}$$

$$\mathcal{F}_2^{\nu N} - x\mathcal{F}_3^{\nu N} = x[u(x) + d(x) + ...] = \overline{q}(x). \tag{54}$$

We expect the quark distribution to display the quasi-elastic peak as in the case of the proton neutron difference, the anti-quark distribution on the other hand is expected to peak towards $x = 0$ since the model is that this is the soft quark anti-quark sea. Both these features are observed as seen in Fig. 19, the data are from the CDHS [16] experiment. The $\mathcal{F}_3$ data are used

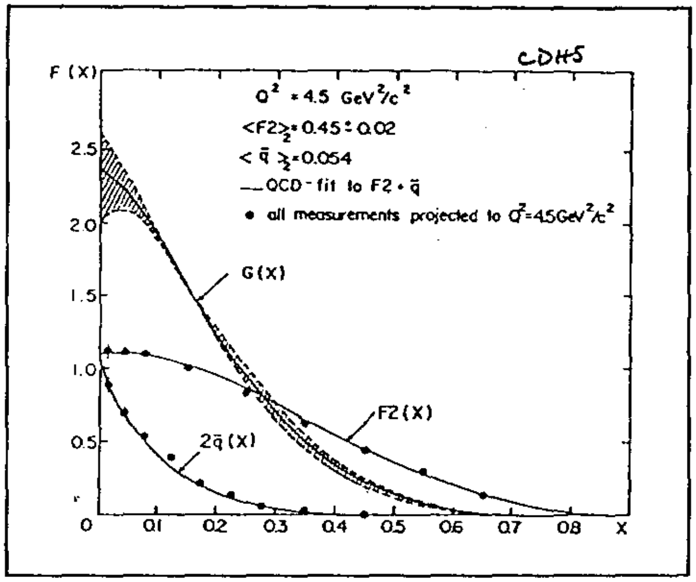

Figure 19: Separation of quark and anti-quark distributions.

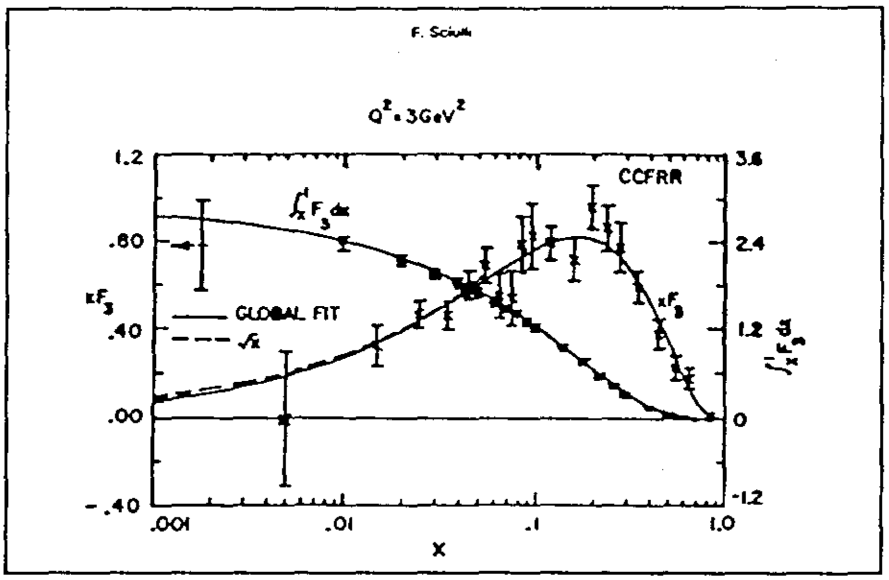

Figure 20: Measurement of $x\mathcal{F}_3$ and related integral.

to check the Gross-LLewellyn-Smith Sum Rule, Eq. 48, and this is shown in Fig. 20, taken from Ref. [14].

2.2.3 Ratio between Charged Lepton and Neutrino Structure Functions

We can compare the structure functions for an isoscalar target and find the rather remarkable result

$$\frac{\mathcal{F}_2^{\mu N}}{\mathcal{F}_2^{\nu N}} \simeq \frac{5}{18}. \tag{55}$$

There are differences in the minority quark distributions which give a correction to this and we see in Fig. 21 that the data are in reasonable agreement with this QPM prediction,

$$\mathcal{F}_2^{\mu N} - \frac{5}{18}\mathcal{F}_2^{\nu N} = \frac{1}{3}(c - s) \tag{56}$$

but at high x, these corrections are negligible.

2.2.4 Determination of the Strange Quark Sea

In neutrino interactions, transitions from the light quarks d, s to charm quarks take place similarly for anti-neutrinos transitions from $\overline{d}$ and $\overline{s}$, although this latter is negligible, to $\overline{c}$. The resulting charm hadrons have large, approximately 10%, branching ratios for the semi-leptonic decay yielding an extra muon in the final state. An extra signature for the charm decay is missing energy corresponding to the final state neutrino. The cross-sections may be written

$$d\sigma^{\nu} = \frac{G^2 M E_\nu x}{\pi}[\mathcal{U}_{cd}^2[u(x) + d(x)] + \mathcal{U}_{cs}^2 2s(x)], \tag{57}$$

$$d\sigma^{\overline{\nu}} = \frac{G^2 M E_\nu x}{\pi}[\mathcal{U}_{cd}^2[\overline{u}(x) + \overline{d}(x)] + \mathcal{U}_{cs}^2 2\overline{s}(x)], \tag{58}$$

where $\mathcal{U}_{cd}^2$ and $\mathcal{U}_{cs}^2$ are the appropriate weak matrix elements, analogous to the Cabbibo angle factors. The experiment has been performed by both the CDHS [17] and CFRR [18] with the result

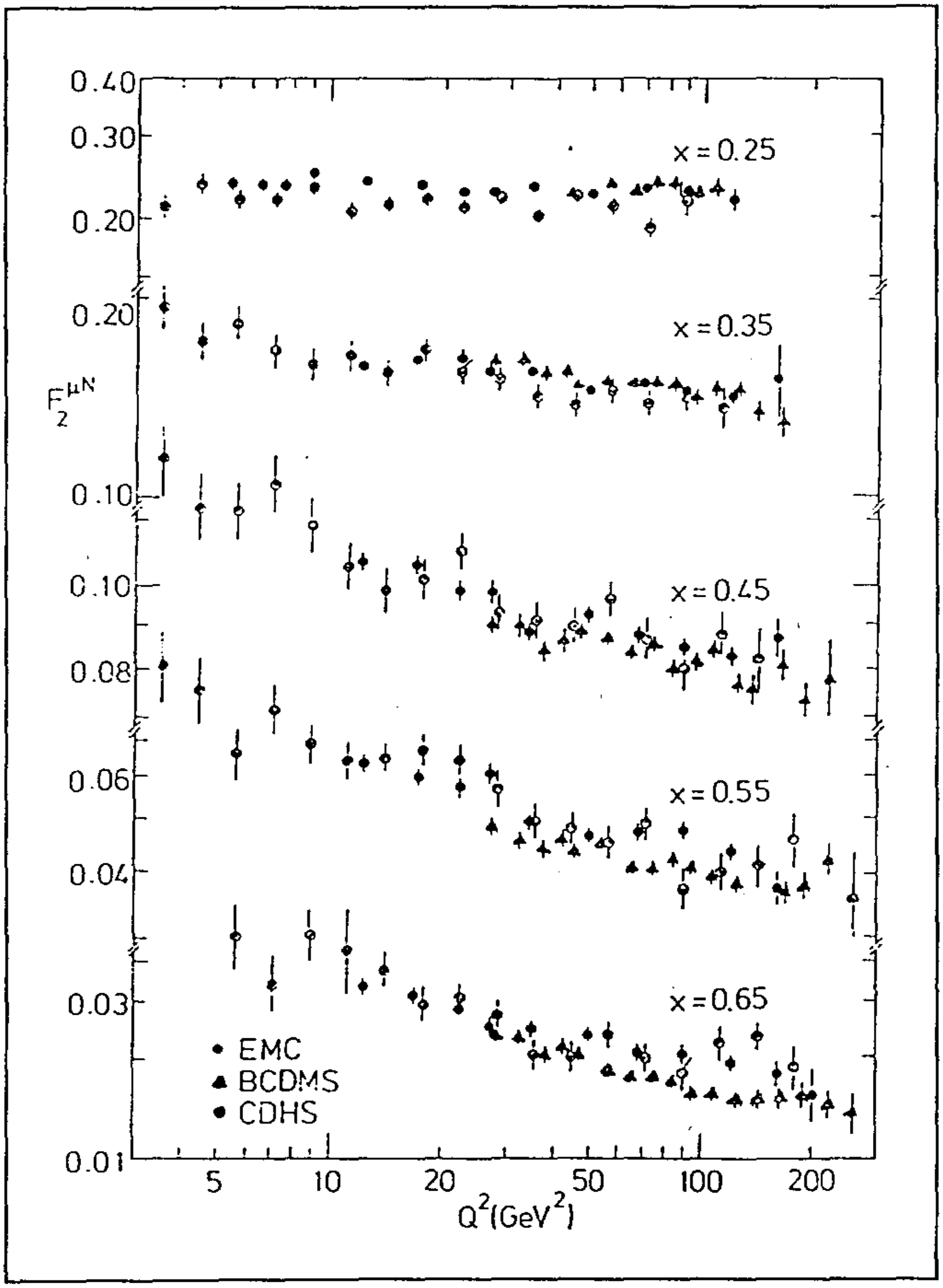

Figure 21: Ratio of Structure Functions from Muon and Neutrino Interactions.

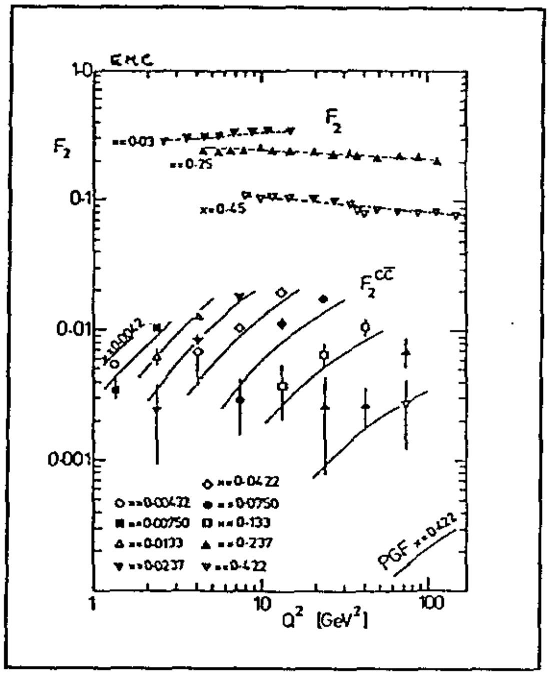

Figure 22: The Non-Scaling Behavior of the Charm Structure Function.

$$\frac{\int x(s+\overline{s})dx}{\int x(\overline{u}+\overline{d})dx} \simeq 0.5. \tag{59}$$

One of the complications which arises in this process is that even if the mass of the strange quark can be considered small, that of the charm quark cannot. (In fact, the result that the Strange Sea is suppressed relative to the u and d sea distributions probably should be interpreted as evidence that the s quark mass is not negligible.) This means that the transitions considered here have a threshold dependence which leads to deviations from a scaling behavior, the notorious Slow Rescaling discussed by Fisk and Sciulli.

2.2.5 Determination of the Charm Quark Sea

In muon interactions, charm production does not proceed by a weak transition rather a charm quark is produced by electromagnetic interaction with a charm sea quark. It is to some extent a matter of semantics as to whether these sea quarks in some way exist in the nucleon or whether they are produced by a mechanism based on the order α_S* photon gluon fusion

*See next Lecture

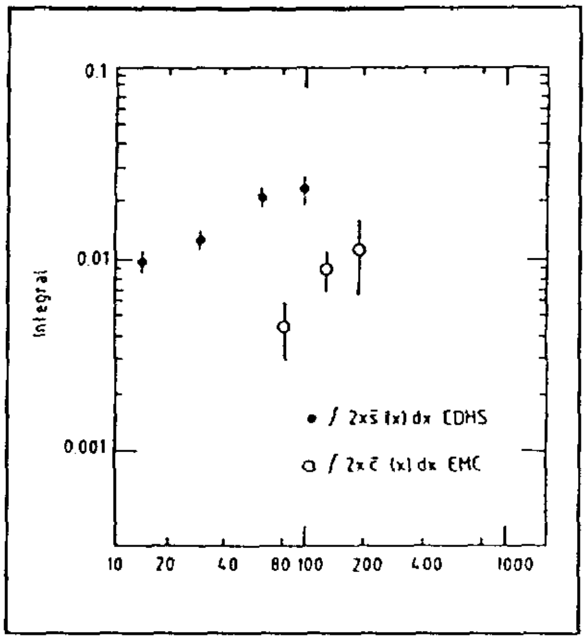

Figure 23: A comparison of the Strange and Charm Quark Sea Distributions.

process. The experimental technique is again to detect the extra muon from the charm hadron decay and the missing energy. This contribution to $\mathcal{F}_2$ is also non-scaling as was first convincingly demonstrated by the Berkeley-Fermilab-Princeton group [19]. The point is illustrated in Fig. 22, which shows data from EMC [20]. The two minority quark seas are compared in Fig. 23, which is taken from Sloan, Smadja and Voss.

2.2.6 Significance and Determination of R

At the beginning of this Lecture we made the identification

$$2x\mathcal{F}_1 = \mathcal{F}_2 = \sum q_i^2 x f(x). \tag{60}$$

If we take this along with Eq. 21 we deduce that in the QPM $\sigma_l = 0$ and hence, $R = 0$. This is a consequence of our derivations which assumed that the quarks had spin $\frac{1}{2}$. Had we worked with spin 0 constituents, we would have obtained $\sigma_t = 0$ and $R = \infty$. R is thus a measure of the spin of the constituents of the nucleon, however, it is more importantly a source of problems for the experimenter. Over the years many attempts have been made to determine R and its dependence on the variables in the problem.

Because it turns out to be relatively small this is a difficult task, on the other hand ignorance of its value casts doubts on any extraction of the structure functions from the cross-sections measured. It would take more time than is available to do justice to the saga of R so I will confine myself to a series of remarks. These are based on the various high energy Neutrino and Muon scattering experiments [16, 21, 23] but also on a recent low energy experiment [22] which made a rather serious measurement at intermediate Q^2.

1. *R is small, lending support to the QPM with spin $\frac{1}{2}$ constituents.*
2. *At intermediate and small Q^2 and at high x, $R \neq 0$, understanding of this requires the introduction of non QPM concepts like intrinsic quark momentum and quark mass effects.*
3. *At small x even at large Q^2, $R \neq 0$. This may be related to the order α_S*† *QCD contributions which are expected. As yet the data are not of sufficient accuracy to make use of these measurements to determine α_S the coupling constant of QCD.*

2.2.7 The Momentum Sum Rule

We have seen how the structure functions are related, with factors coming from either the weak or electromagnetic charges, to the momentum distributions of the quark. If the quarks were to carry all of the momentum then we would expect,

$$\int \mathcal{F}_2{}^{\nu\mathcal{N}} = (1-\epsilon) \tag{61}$$

for neutrinos and

$$\frac{18}{5}\int \mathcal{F}_2{}^{\mu\mathcal{N}} = (1-\epsilon) \tag{62}$$

for charged leptons, with $\epsilon = 0$. Since the early '70s the value for ϵ has been measured to be about 0.5. That is to say that 50% of the momentum of the proton is not carried by the quarks. The first responses to this fact

† See next Lecture

suggested that perhaps there were some neutral (no electromagnetic or weak couplings) constituents of the nucleon which perhaps bound the ensemble of quarks together. This is the origin of the term Gluon which, if memory is correct, preceded the formal proposals of QCD. It will be from this point that we start the next Lecture.

3 Lecture III

3.1 Introduction

We finished the last Lecture with the fact that the fraction of the proton's momentum, which is carried by the charged quarks, is approximately 50%. During the early '70s there were theoretical developments, in some part prompted by the deep inelastic data which led to the formulation of Quantum Chromodynamics and its emergence as the strongest candidate theory of strong interactions. In simple terms quarks are considered to carry a color quantum number and to interact with each other through the exchange of gluons. There is a close analogy with quantum electrodynamics with the charged leptons being replaced by the quarks and the photons replaced by gluons. The major difference is that the coupling constant evolves as a function of momentum transfer scale in such a manner as to reduce the strength of the coupling and lead to essentially free partons at asymptotically high Q^2. That is, the QPM may be considered as the high energy limit of QCD. At finite energies the theory predicts deviations from strict scaling behavior and it is these aspects which we will attempt to elucidate in this Lecture.

3.2 Quantum Chromodynamic Evolution

Let us consider the process

$$\gamma + q \rightarrow q + g. \tag{63}$$

We can write the cross section,

$$\frac{d\sigma_1}{dp_t{}^2} = [\frac{4\pi^2\alpha}{W^2}]e_i{}^2 \frac{1}{p_t{}^2}\frac{\alpha_S}{2\pi}\frac{4}{3}(\frac{1+z^2}{1-z}), \tag{64}$$

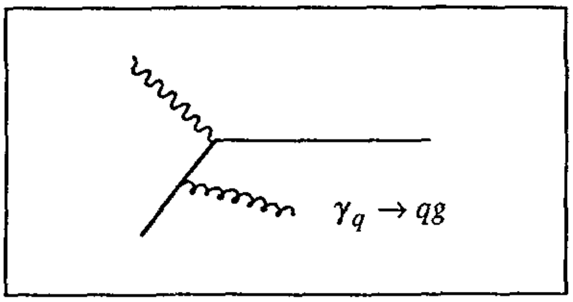

Figure 24: The process $\gamma + q \to q + g$.

z is the fraction of the energy of the collision carried by the gluon. From the relationships already considered we can recognize

$$\mathcal{F}_1 = \frac{W^2}{4\pi^2\alpha^2}\sigma_t = \frac{\mathcal{F}_2}{x}, \tag{65}$$

which permits us to make the definition $\sigma_0 \equiv \frac{W^2}{4\pi^2\alpha}$. We can also recognize a singularity at $p_t{}^2 = 0$, that is to say, the process has a forward peak, and in the $\frac{4}{3}(\frac{1+z^2}{1-z})$ term there is singularity for zero energy gluon emission, the so-called infra red divergence. The factor $\frac{4}{3}$ comes from the Clebsch-Gordon coefficients of color and the whole term, since it describes the collinear process $q \to q + g$, is called a splitting function P_{qq}. We can then rewrite the full expression

$$\frac{d\sigma_1}{dp_t{}^2} = \sigma_0 e_i{}^2 \frac{1}{p_t{}^2}\frac{\alpha_S}{2\pi}P_{qq}. \tag{66}$$

If we integrate over $p_t{}^2$, we find

$$\sigma_1 = \sigma_0 e_i{}^2 \frac{\alpha_S}{2\pi}P_{qq}\int_{\mu^2}^{p_t{}^2{}_{max}} \frac{dp_t{}^2}{p_t{}^2}, \tag{67}$$

$$\sigma_1 = \sigma_0 e_i{}^2 \frac{\alpha_S}{2\pi}P_{qq}\ln\frac{p_t{}^2{}_{max}}{\mu^2}. \tag{68}$$

Up to this stage we have used the variable $p_t{}^2$, in order to use, instead, the variable Q^2, we have to scramble a little. One way is to write

$$p_{t_{max}}^2 = Q^2\frac{1-z}{4z}, \tag{69}$$

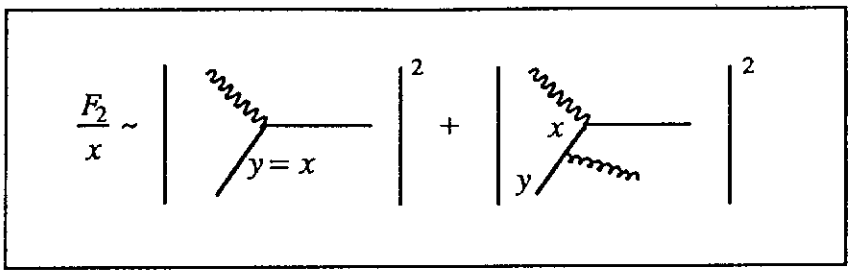

Figure 25: Diagrammatic version of the correction to $\mathcal{F}_2$.

then

$$\ln p_{t_{max}}^2 = \ln Q^2 + \ln \frac{1-z}{4z} \simeq \ln Q^2, \tag{70}$$

for Q^2 large. We are then permitted to conclude

$$\sigma_1 = \sigma_0 e_i{}^2 \frac{\alpha_S}{2\pi} P_{qq} \ln \frac{Q^2}{\mu^2}, \tag{71}$$

at which point we see that we have some Q^2 dependence, the data are certainly not scaling exactly, and this Q^2 dependence is only logarithmic which is also good since the Q^2 dependence in the data, as we have seen, is not dramatic.

At this stage we should pause and reflect. We consider the suggestion that what we have just calculated could be the first order correction to the parton model.

Diagrammatically, we have the situation shown in Fig. 25, algebraically, we have:

$$\frac{\mathcal{F}_2}{x} = \Sigma e_i{}^2 \int_x^1 \frac{dy}{y} q(y)(\delta(1-\frac{x}{y}) + \frac{\alpha_S}{2\pi} P_{qq}(\frac{x}{y}) \ln \frac{Q^2}{\mu^2}). \tag{72}$$

The first term in this equation, that containing the integral over the δ function, clearly represents the simple parton model. We can thus rewrite the equation as

$$\frac{\mathcal{F}_2}{x} = \Sigma e_i{}^2 [q(x) + \Delta q(x)], \tag{73}$$

where we have defined

$$\Delta q(x,Q^2) = \frac{\alpha_S}{2\pi}\ln\frac{Q^2}{\mu^2}\int_x^1 \frac{dy}{y} P_{qq}(\frac{x}{y}) q(y). \tag{74}$$

We then note that the Q^2 dependence in the equation is entirely contained in the Δq, indeed

$$\frac{dq(x,Q^2)}{d\ln Q^2} = \frac{\alpha_S}{2\pi}\int_x^1 \frac{dy}{y} P_{qq}(\frac{x}{y}) q(y,Q^2). \tag{75}$$

Now we can rewrite

$$q(x,Q^2) = [q(x) + \Delta q(x)], \tag{76}$$

$$q(x,Q^2) = \int_0^1 dy \int_0^1 dz q(y,Q^2)[\delta(1-z) + \frac{\alpha_S}{2\pi}\mathcal{P}_{qq}(z)\ln(\frac{Q^2}{\mu^2})]\delta(x-yz), \tag{77}$$

where the term in square brackets can be interpreted as the probability density to find a quark inside a quark carrying a fraction z of the original quarks momentum.

I hope that the reader gradually sees the emergence of the concept that as Q^2 rises we see deeper and deeper into the interior of the quark. This is basically the analogy of the treatment of the QED case, usually attributed to Weizacker and Williams. (Actually, I have looked at the Physical Review paper usually quoted and I do not find the connection transparent.)

At this stage, however, there is a problem with our putative interpretation of the square bracket as a probability density because we should notice that the probability for a quark to be something, itself or another quark, now exceeds unity. We are also ignoring other diagrams such as those shown in Fig. 26.

The inclusion of these diagrams helps and using conservation of probability we obtain:

$$\mathcal{P}_{qq}(z) = \frac{4}{3}[\frac{1+z^2}{(1-z)_+} + \frac{3}{2}\delta(1-z)], \tag{78}$$

and

$$\frac{d\ln q(x,Q^2)}{d\ln Q^2} = \frac{\alpha_S}{2\pi}\frac{1}{q(x,Q^2)}\int_x^1 \frac{dy}{y} P_{qq}(\frac{x}{y}) q(y,Q^2). \tag{79}$$

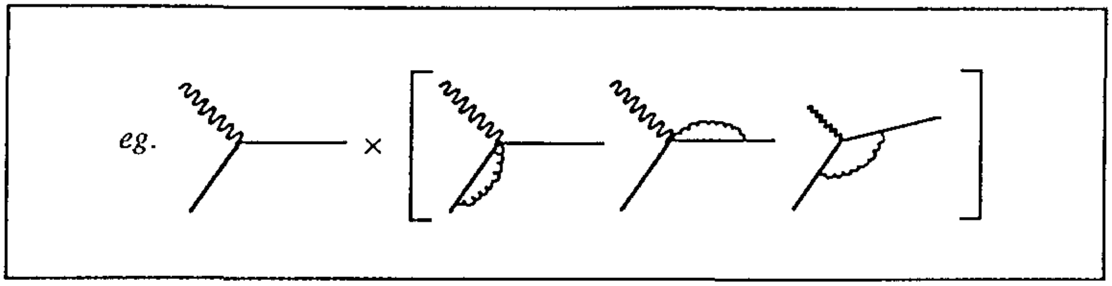

Figure 26: Other diagrams contributing to the process.

which constitutes the final result of our labour.

3.3 A Toy QCD Analysis

The question now arises, "So What?", "Can we do anything with this result?" We first note that none of the diagrams we have calculated corresponds to a gluon splitting into a quark-antiquark pair. Such a diagram would contribute to any "sea " quantity and so our question can be rephrased..." Do we have any observables which do NOT contain a sea quark component?" The answer is "YES", we have the difference between $\mathcal{F}_2{}^p$ and $\mathcal{F}_2{}^n$, we have $\mathcal{F}_2$ at high x where the contribution from the sea quarks becomes negligible. From neutrinos we have the quantity $x\mathcal{F}_3$, which is obtained by taking a difference between neutrino and antineutrino structure functions. From our result, if the data are presented in the same form as our left-hand side, we only have to perform some simple integrals to see whether we can describe the data and perhaps to obtain an estimate of the QCD scale parameter.

Now, in my normal life, I do not evaluate quantities with the subscript"+" every day so I looked for help. Keith Ellis explained it to me, in words of one syllable or less, and talked me through the integrations before leaving for the latest hot conference. I used a parameterization $\mathcal{F}_2{}^\mu = 0.35(1-x)^3$ which used to serve well for rate estimations in the early seventies and went to work. After a couple of days I admitted defeat by one integral and did that one numerically on a piece of paper but did the rest analytically and found that at $x = 0.7$ and with $\alpha_S = 0.2$, I obtained $\frac{d\ln\mathcal{F}_2}{d\ln Q^2} = -0.172$. The data from the BCDMS muon scattering experiment are shown in the figure

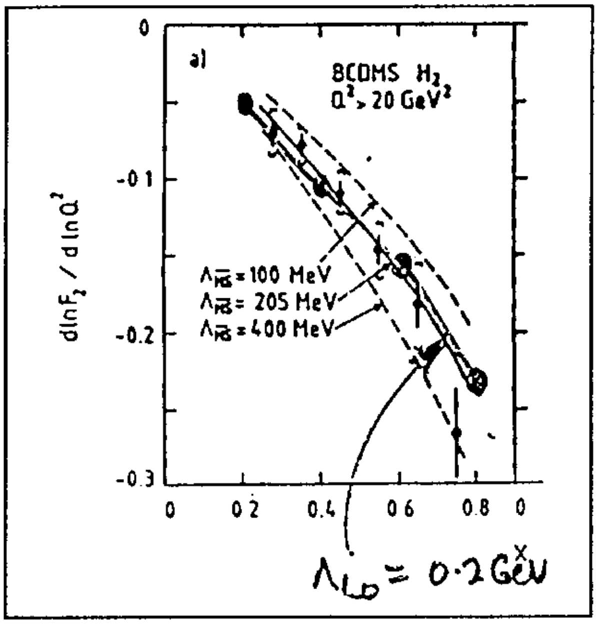

Figure 27: Muon Scattering Data Described by the Toy Model.

and we see that the sign is correct and that the data are at about -0.2. This was very tempting so I became theoretician for a day and wrote a little 2 page fortran program which would calculate other x values and use other functions. I obtained the heavy line through the BCDMS data with $\Lambda = 0.2$ *GeV* and obtained the line shown in the next figure through a preliminary version of the Fermilab E744/770 neutrino experiment data for $x\mathcal{F}_3$.

Admittedly the data are already slopes of the actual $\mathcal{F}$ measurements but it is quite remarkable how directly one goes from the data to an estimate of one of the fundamental parameters of one of the fundamental interactions, one of the four known forces.

3.4 The Running Coupling Constant

In all the above derivation we assumed that α_S is a constant number, this is only an approximation. The coupling constant for QED , α_{QED} varies because of diagrams such as those which include lepton loops in the photon propagator. The coupling constant of QCD also runs but in this case the higher order diagrams include also those which involve three gluon vertices. The photon is electrically neutral but the gluon has a color charge which

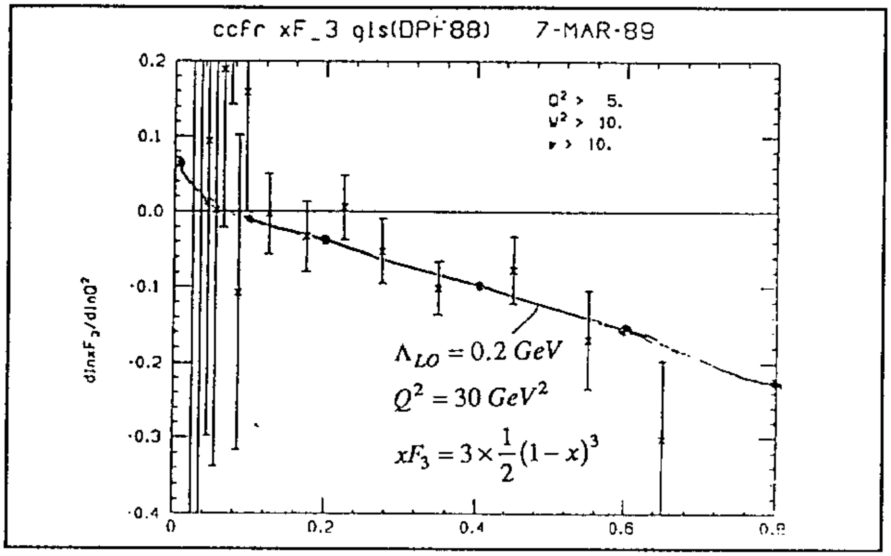

Figure 28: Neutrino Data Described by the Toy Model.

introduces these extra diagrams. It is the presence of these and others which lead to the variation of α_S with Q^2 according to the expression

$$\alpha_S(Q^2) = \frac{12\pi}{(33 - 2n_f)\ln\frac{Q^2}{\Lambda^2}}. \tag{80}$$

We should note that this expression implies that α_S falls with increasing Q^2 and, hence, that at high Q^2 we might expect perturbation theory to work. Either α_S or the mass parameter Λ may be taken as a free parameter of the theory. In order to incorporate the running of the coupling constant in the preceding formulae it is sufficient to replace the constant α_S with the Q^2 dependent expression. One interesting point is that the double logarithmic derivative of the structure function, $\frac{d\ln\mathcal{F}_2}{d\ln\ln Q^2}$, then contains less explicit Q^2 dependence and should perhaps be used for comparison between data and theory. This distinction between double and single logarithmic derivative is not yet evident in the data.

3.5 Real QCD Analyses

Real QCD analyses of deep inelastic scattering data in fact use all the splitting functions of quarks and gluons. In addition to the P_{qq}, which we employed above, there are P_{qG}, the probability distribution of a gluon in a quark, P_{Gq}, the probability distribution of a quark or anti-quark in a gluon and P_{GG}, the probability distribution of a gluon in a gluon. All the formulae are derived to next to leading order in α_S and the numerical apparatus for fitting the data is very non-trivial.

As given by Altarelli and Parisi [24] an appropriate set of evolution equations for quark and gluon distributions is:

$$\frac{d}{d\ln Q^2}q(x,Q^2) = \frac{\alpha_S(Q^2)}{2\pi}\int_x^1 \frac{dy}{y}[q_i(y,Q^2)P_{qq}(\frac{x}{y}) + G(y,Q^2)P_{qG}(\frac{x}{y})] \quad (81)$$

$$\frac{d}{d\ln Q^2}G(x,Q^2) = \frac{\alpha_S(Q^2)}{2\pi}\int_x^1 \frac{dy}{y}[q_i(y,Q^2)P_{Gq}(\frac{x}{y}) + G(y,Q^2)P_{GG}(\frac{x}{y})]. \quad (82)$$

The equivalent expressions for the electron-photon case, the "Weizacker-Williams" approximation are given by Chen and Zerwas [25]. Typical fits using this form are shown to some EMC data in Figs. 29 and 30. In the first, the data are all at $x > 0.25$ and the non-singlet (no gluon) expressions are used, in the second, data down to fairly low x are used and the full expression including the singlet terms, both quark and gluon splitting functions, were used.

Data from neutrinos and antineutrinos in the same experiment give an extra handle on the equations and this is often employed to get a handle on the Gluon distribution. A particular example of this is the analysis performed by the CDHS [7] group. They rewrite the Altarelli-Parisi equations in the form

$$\frac{d}{d\ln Q^2}\mathcal{F}_2(x,Q^2) = \frac{\alpha_S(Q^2)}{2\pi}\int_x^1 \frac{dy}{y^2}[\mathcal{F}_2(y,Q^2)P_{qq}(\frac{x}{y}) + 2N_{F_2}G(y,Q^2)P_{qG}(\frac{x}{y})] \quad (83)$$

$$\frac{d}{d\ln Q^2}\overline{q}(x,Q^2) = \frac{\alpha_S(Q^2)}{2\pi}\int_x^1 \frac{dy}{y^2}[\overline{q}(y,Q^2)P_{qq}(\frac{x}{y}) + N_{\overline{q}}G(y,Q^2)P_{qG}(\frac{x}{y})] \quad (84)$$

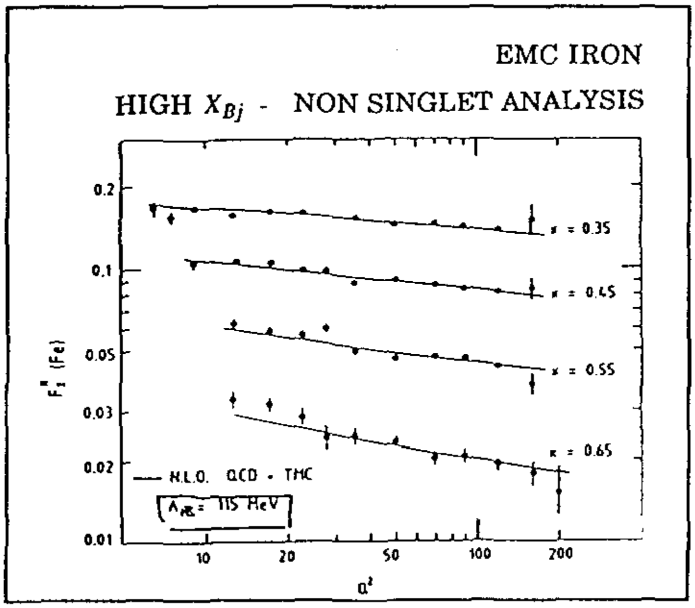

Figure 29: An Example of a Non-Singlet QCD fit to muon scattering data.

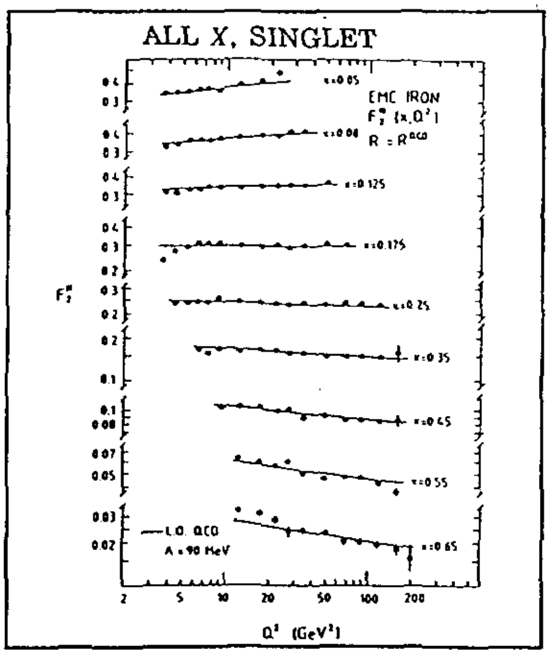

Figure 30: An Example of a Singlet QCD fit to muon scattering data.

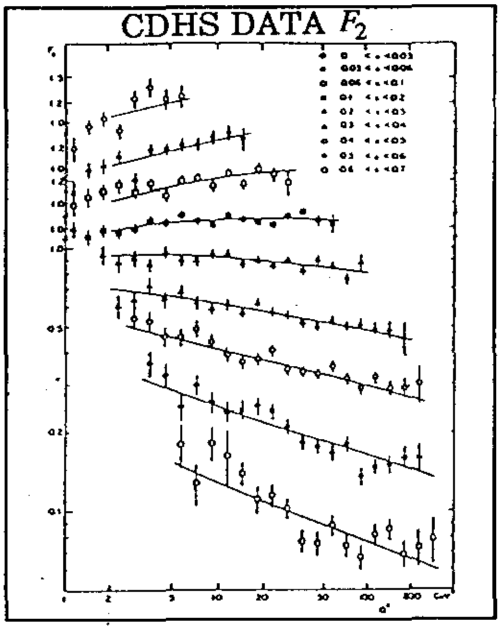

Figure 31: CDHS Neutrino Data on F_2 fitted by QCD.

$$\frac{d}{d\ln Q^2}G(x,Q^2) = \frac{\alpha_S(Q^2)}{2\pi}\int_x^1 \frac{dy}{y^2}[\mathcal{F}_2(y,Q^2)P_{qG}(\frac{x}{y}) + G(y,Q^2)P_{qG}(\frac{x}{y})] \quad (85)$$

where $N_{F_2} = N_{\overline{q}} = 4$. The measured quantities are $\overline{q}(x,Q^2)$ and $\mathcal{F}_2(x,Q^2)$ and the analysis permits the determination of Λ_{LO} and $G(x,{Q_0}^2)$. The fitting is performed by parameterizing the actual distributions and that of the gluon. There is some importance to the choice of the parameterization for the gluon distribution and there is no possibility to compare directly with the data for that distribution.

The fits to the data are shown in Figs. 30 - 34, which display both the data themselves and the derivatives of the data with respect to Q^2. Finally, Fig. 35 shows the form of the different distributions at $Q^2 = 22.5\ GeV^2$. One immediately notes that both the anti-quark and gluon distributions are much more peaked to low x than the F_2 distribution. The fit to the data is quite good, the fraction of momentum carried by the gluons comes out to be 0.55 ± 0.11.

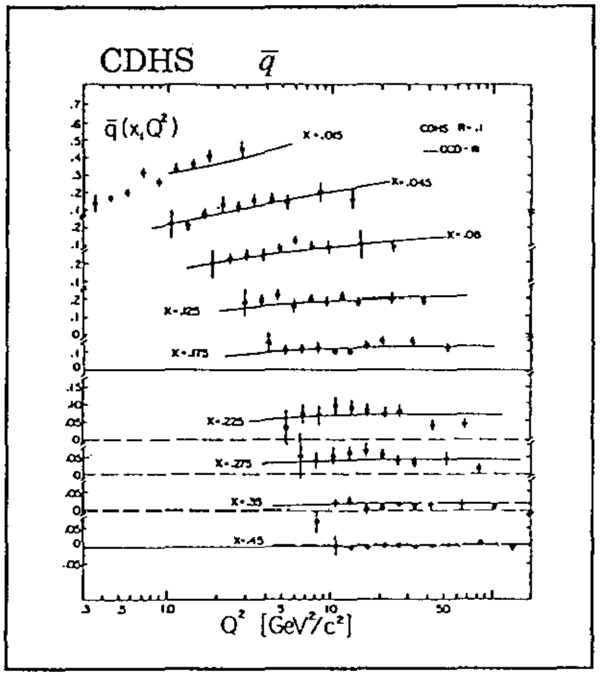

Figure 32: CDHS Neutrino Data on $\overline{q}$ fitted by QCD.

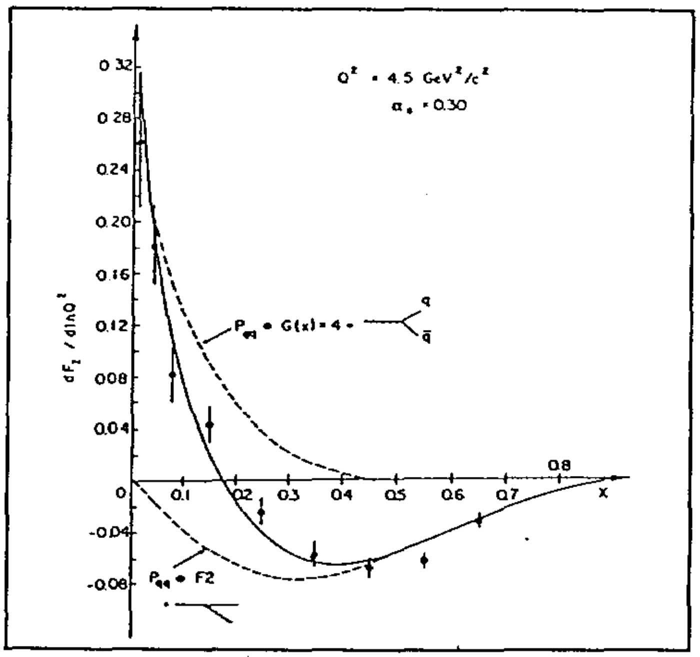

Figure 33: CDHS Neutrino Data on the Q^2 dependence of F_2 showing the contributions of the different splittings.

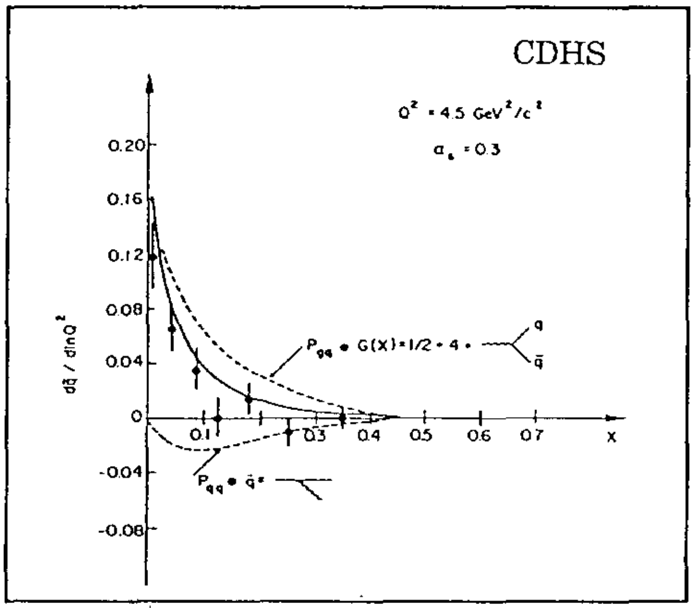

Figure 34: CDHS Neutrino Data on the Q^2 dependence of $\overline{q}$ showing the contributions of the different splittings.

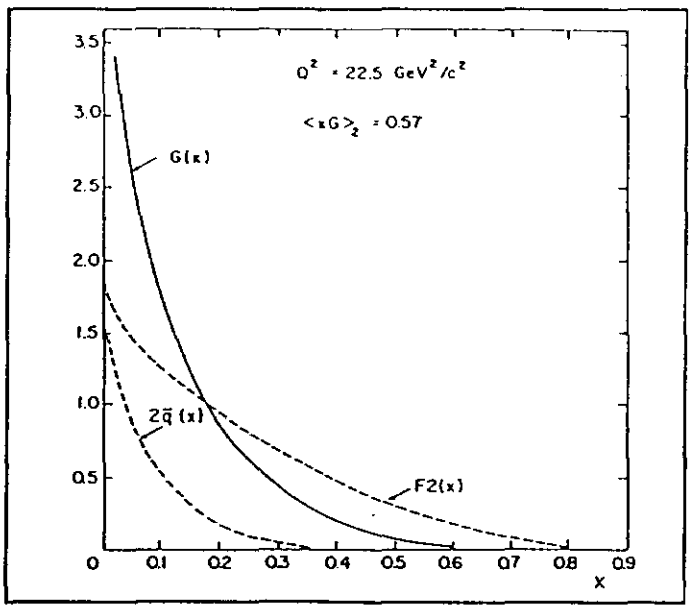

Figure 35: Functions Resulting from QCD fits to CDHS Neutrino Data.

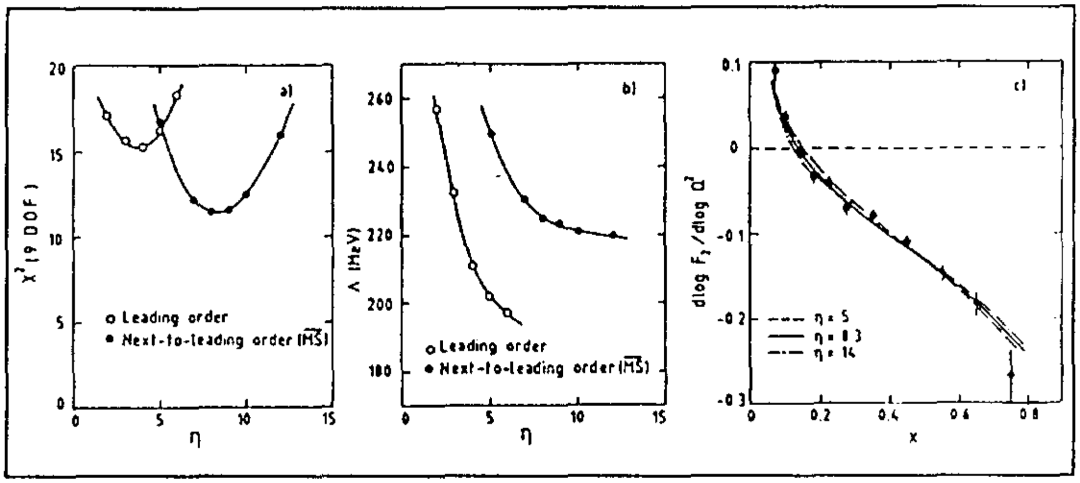

Figure 36: Sensitivity of the BCDMS QCD Fits to the Gluon Distribution.

3.6 Gluon Distribution

In the previous sub-section we concluded with the indication that although the gluon distribution does not appear as a direct observable in inclusive neutrino scattering, there are combinations of the structure functions whose evolutions are affected by the gluon distribution and some measure can be obtained. A similar situation exists in muon scattering. There is not the additional help analogous to the use of neutrinos and anti-neutrinos, everything must be done from the evolution of the single structure function F_2. Until recently the data were not of sufficiently high statistics to achieve anything. The recent BCDMS data [23] has very high statistics and they have demonstrated that their data can in fact give a determination of the parameters of a gluon distribution PROVIDED A SUFFICIENTLY SIMPLE PARAMETERIZATION IS IMPOSED.

This is shown in Fig. 36, readers can judge for themselves from the rightmost sub-figure how difficult is this determination. The results along with a determination by the EMC group are shown in Fig. 37. The EMC group used a completely different method in order to obtain the gluon distribution. The

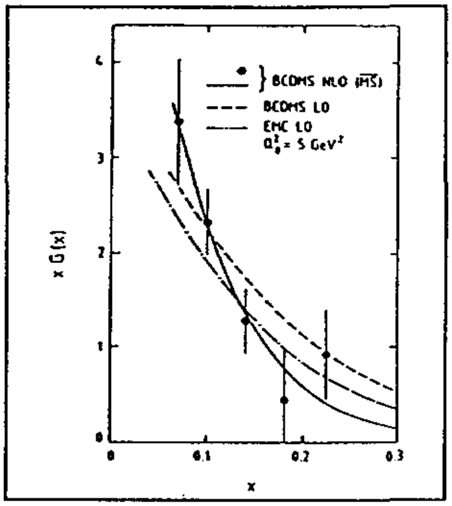

Figure 37: Results from BCDMS and EMC on the Gluon Distribution.

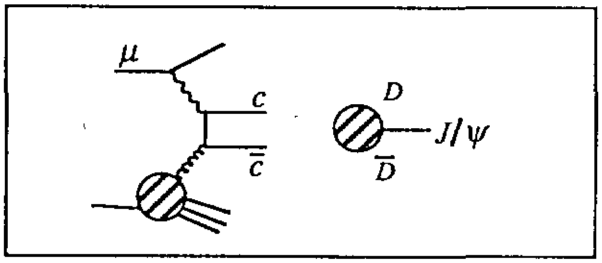

Figure 38: Photon-gluon fusion Diagram for J/ψ production indicating sensitivity to the gluon distribution.

modern models of J/ψ production involve the photon-gluon fusion diagram, Fig. 38. The process as shown is then sensitive to the gluon distribution in the nucleon. The measurements were performed with an iron calorimeter target and the signal, see Fig. 39, was extracted using the peak in the dimuon mass distribution in dimuon and trimuon events.

Similar results were obtained by the Berkeley-Fermilab-Princeton experiment at Fermilab. Again, as shown, the data give some determination of the gluon distribution, however, there are ongoing discussions about the model dependence of such a measurement.

One of the problems is that the data are also sensitive to the mass chosen within the model for the charm quark. Finally, in Fig. 41, I show a collection of different functional representations of the gluon distribution from different measurements. It should be noted that in few of these cases do we have a

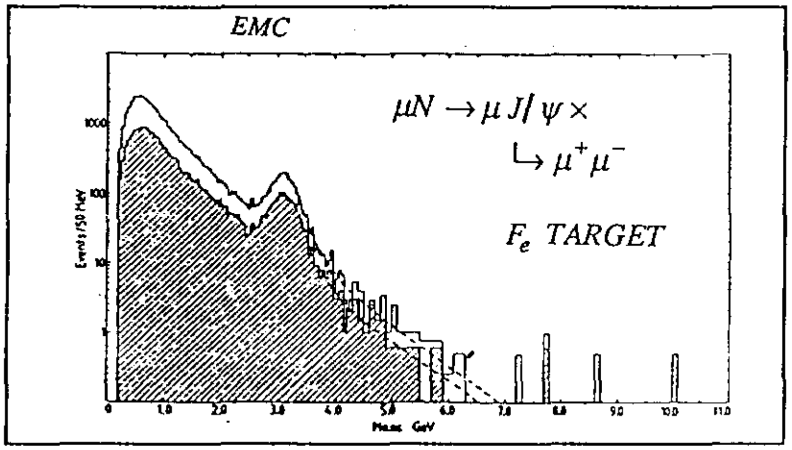

Figure 39: Dimuon mass distributions showing the J/ψ signal.

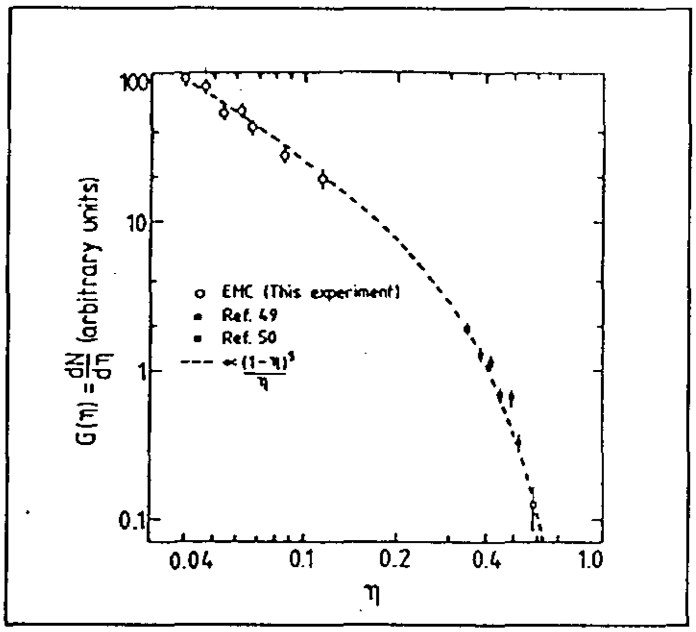

Figure 40: Gluon distribution obtained from J/ψ production.

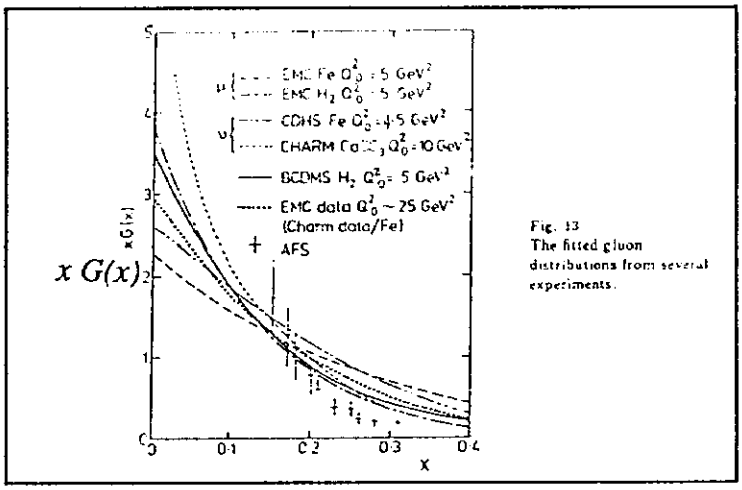

Figure 41: A collection of gluon distributions obtained by different methods.

point by point determination.

Included in this collection is a measurement from the Axial Field Spectrometer (AFS) at the CERN ISR. I mention this because it was obtained from a measurement of the single photon production cross-section in pp scattering. In principle, such measurements [26, 27, 28] provide a good opportunity to determine this most elusive of parton distributions. Unfortunately to date [28], none of the data cover a sufficiently wide range of kinematic variable to more than, once again, determine the single parameter of a very simple representative function.

3.7 Concluding Remarks on QCD Analyses

In this Lecture, we have attempted to proceed from a derivation of the expected Q^2 dependence of QCD corrections to the quark parton model, through a simple demonstration that such corrections describe the data rather nicely, to a discussion of the kinds of results that may be obtained from a fully fledged analysis of the data. It should be emphasized that there are a number of sophistications associated with a real analysis which I have not dwelt on here, at least not in this written version. The statistical accuracy of the data has improved over the last decade to such an extent that small systematic differences between data sets assume high importance, a fit understands statistics, it does not understand systematics. Further, there may be differences in what each group actually defines as a structure func-

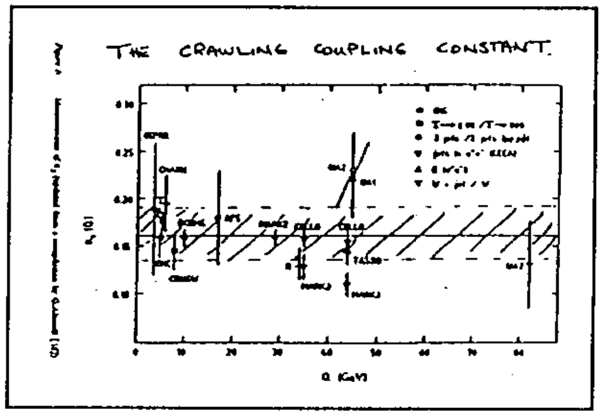

Figure 42: The Crawling Coupling Constant.

tion, there are some corrections traditionally made by one group which are traditionally not made by another group. This and other detailed aspects of the data were discussed at Snowmass [4] and as a result there are new analyses of combined data sets from different measurements [29] which attempt to take into account, at some level, systematic errors. I would be less than honest, however, if I did not say that I feel that the state of agreement between experiments is not satisfactory. Nevertheless, deep inelastic scattering remains one of the best sources of information on the scale and behaviour of the strong interaction, the mass scale in the coupling constant has been rather reliably determined to be about 100 MeV with errors of about 70 MeV whereas 15 years ago the data, such as they were, suggested about 750 MeV.

Finally, for the strictly QCD aspects of the field we are still lacking a convincing demonstration of the running of the QCD coupling constant. Fig. 42 of this Section shows a collection of recent determinations of α_S. It is clear that within errors a constant value is compatible with the data. This should set the scale of ambition for any future proposals for experiments and indeed the need for a good experiment in this area has been recognised [11, 12] and may be acted on.

4 Lecture IV

In this final Lecture I am in something of a quandary since there are many interesting aspects of recent deep inelastic experimentation which deserve

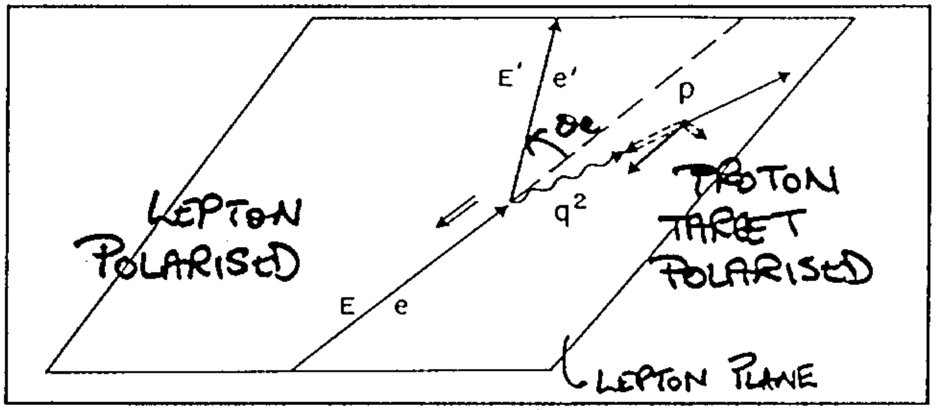

Figure 43: Diagram of polarized lepton scattering.

discussion. On the other hand, it is the final Lecture and we cannot cover everything. I have therefore chosen to address, although perforce somewhat superficially, on the one hand the measurement of polarized proton structure functions and the spin of the proton, and on the other hand some aspects of results of measurements of unpolarized structure functions using nuclear targets.

4.1 Spin Distributions

An extensive review, both theoretical and experimental is given by Hughes and Kuti [30] and the thesis of Papavassilliou [31] contains a description of the recent measurements which have restirred interest in the subject.

Given only electromagnetic interactions (as distinct from weak, or interference of weak and electromagnetic), it is necessary for both incident particle and target particle to be polarized for there to exist an observable due to the polarization. One or the other is not sufficient. The scattering of polarized leptons is significantly more involved in terms of formal notation than is the unpolarized case. We will therefore not proceed in as much detail as in Lecture I. On the other hand the quark parton model picture of what is going on is rather straightforward and some examples will provide considerable insight.

The kinematic situation is shown in Fig. 43, we will consider the case of the lepton polarized parallel or anti-parallel to its direction and, similarly, the proton target polarized parallel or anti-parallel to the lepton direction.

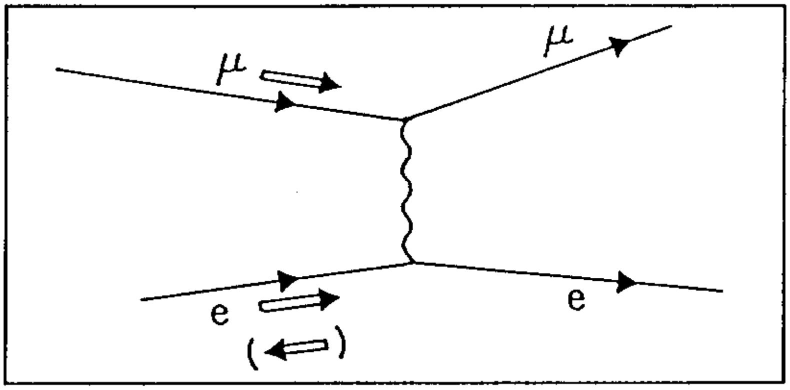

Figure 44: Polarized muon scattering from polarized electron.

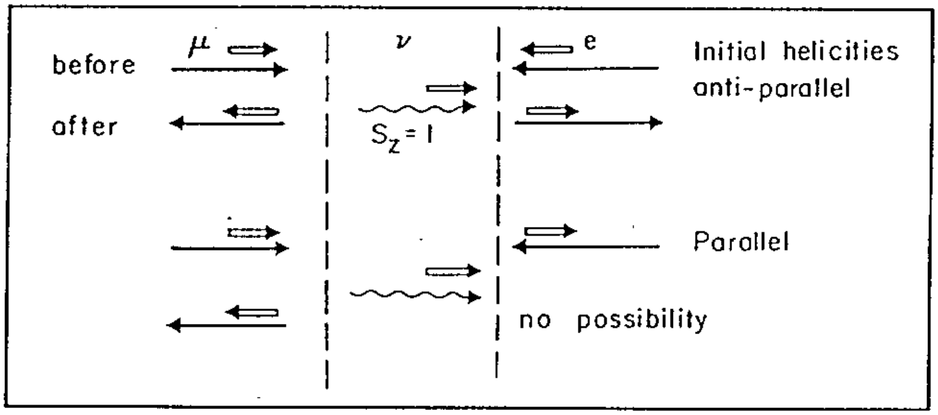

Figure 45: Breit frame picture of the scattering process.

Let us now consider the case of polarized muon scattering from polarized electron by the exchange of the, by now familiar, single virtual photon, Fig. 44.

In the Breit frame, Fig. 45, we can immediately understand that there are some orientations of spin or helicity which just cannot proceed by the single photon exchange mechanism.

We can now see if we can calculate the cross-section following the same methods as for the unpolarized case. We introduce again the lepton tensor and the hadron tensor and to account for the polarization of the particles we have included the spin projection operators containing their γ_5 terms.

The presence of this γ_5 introduces an antisymmetric part in the lepton

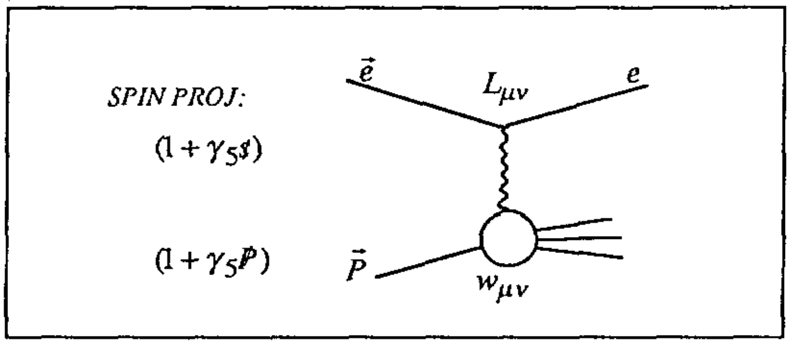

Figure 46: Diagram for polarized lepton scattering from polarized target.

tensor,

$$\mathcal{L}_{\mu\nu} = \mathcal{L}_{\mu\nu}{}^S + \mathcal{L}_{\mu\nu}{}^A \tag{86}$$

and in the hadron tensor,

$$\mathcal{W}_{\mu\nu} = \mathcal{W}_{\mu\nu}{}^S + \mathcal{W}_{\mu\nu}{}^A. \tag{87}$$

Contracting, we get finite terms only for the SS and AA combinations, the former lead to the normal unpolarized structure functions $\mathcal{W}_1$ and $\mathcal{W}_2$. The product of the antisymmetric parts leads to two new structure functions $\mathcal{G}_1$ and $\mathcal{G}_2$. This constitutes a demonstration that polarization of BOTH beam and target is necessary.

$$\mathcal{L}^{\mu\nu}\mathcal{W}_{\mu\nu} = {}^S\mathcal{L}^{\mu\nu}\mathcal{W}_{\mu\nu}{}^S + {}^A\mathcal{L}^{\mu\nu}\mathcal{W}_{\mu\nu}{}^A. \tag{88}$$

If we now take the sum and the difference of the cross-sections for scattering with the beam and target polarized anti-parallel ($\uparrow\downarrow$) and parallel ($\uparrow\uparrow$) we find for the sum Eq. 20 multiplied by 2,

$$\frac{d^2\sigma}{d\Omega dE'}(\uparrow\downarrow + \uparrow\uparrow) = \frac{8\pi\alpha^2(E')^2}{Q^4}[\cos^2(\theta/2)\mathcal{W}_2(\nu, Q^2) + 2\sin^2(\theta/2)\mathcal{W}_1(\nu, Q^2)] \tag{89}$$

and for the difference,

$$\frac{d^2\sigma}{d\Omega dE'}(\uparrow\downarrow - \uparrow\uparrow) = \frac{4\pi\alpha^2 E'}{EQ^2}[(E + E'\cos\theta)MG_1 - Q^2G_2] \tag{90}$$

where G_1 and G_2 are functions of Q^2 and ν as is the case for the unpolarized structure functions. The asymmetry given by the difference divided by the sum can now be written,

$$\mathcal{A} = 2\tan^2(\theta/2)\frac{[(E + E'\cos\theta)MG_1 - Q^2G_2]}{[W_2 + 2W_1\tan^2(\theta/2)]}. \tag{91}$$

In the Bjorken scaling limit these structure functions scale as

$$M^2\nu G_1(Q^2,\nu) \rightarrow g_1(x) \text{ and } M\nu^2 G_2(Q^2,\nu) \rightarrow g_2(x).$$

As with the unpolarized case we can talk in terms of the virtual photon, in this case the virtual photon asymmetries rather than the cross-sections,

$$\mathcal{A} = \mathcal{D}(\mathcal{A}_1 + \eta\mathcal{A}_2), \tag{92}$$

where

$$\mathcal{A}_1 = (\sigma_{\frac{1}{2}} - \sigma_{\frac{3}{2}})/(\sigma_{\frac{1}{2}} + \sigma_{\frac{3}{2}}) \simeq 2xg_1/\mathcal{F}_2, \tag{93}$$

and

$$\mathcal{A}_2 = \sigma_{TL}/(\sigma_{\frac{1}{2}} + \sigma_{\frac{3}{2}}). \tag{94}$$

$\mathcal{D} = E - E'\epsilon/E(1 + \epsilon R)$ is known as the depolarization factor, it is a measure of the photon polarization as compared to the lepton polarization. In the expression for A_2, σ_{TL} denotes an interference between transverse and longitudinal photon states. The factor η is a kinematic factor which in most of the practical cases considered so far is very small and leads us to ignore the contribution of $\mathcal{A}_2$.

4.2 Polarization in the Quark Parton Model

We now take our results for polarized muon electron scattering and apply them to the simple quark model, in the Breit frame as represented in Fig. 47.

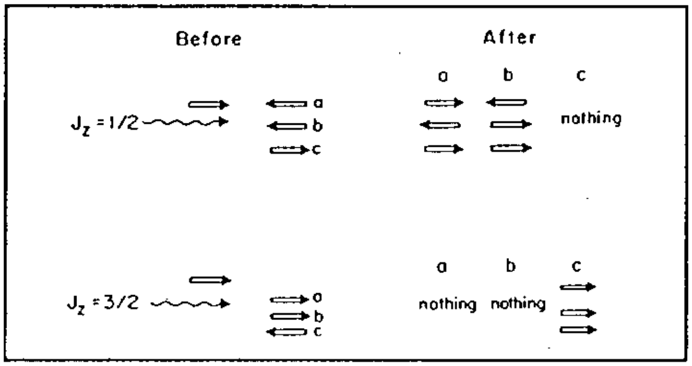

Figure 47: Polarized Scattering in Simple Quark Model in the Breit Frame.

Again, noting those final states which are permitted and those which are not, for the different initial polarization states of photon and proton, we can write

$$\sigma_{\frac{1}{2}} \simeq \Sigma_i {e_i}^2 q_i(\uparrow) \tag{95}$$

$$\sigma_{\frac{3}{2}} \simeq \Sigma_i {e_i}^2 q_i(\downarrow) \tag{96}$$

which leads us to the result,

$$\mathcal{A}_1 = \frac{\Sigma_i e_i^2 (q_i(\uparrow) - q_i(\downarrow))}{\Sigma_i e_i^2 (q_i(\uparrow) + q_i(\downarrow))} \equiv 2x g_1/\mathcal{F}_2. \tag{97}$$

If we use the $SU(6)$ symmetric wave function for the nucleon and ignore the quark-anti-quark sea then we obtain ${\mathcal{A}_1}^p = \frac{5}{9}$ and $\mathcal{A}_1^n = 0$ [32]. Let us develop the quark parton model result further, we have

$$2\int g_1(x)dx = \Sigma_i {e_i}^2 (q_i(\uparrow) - q_i(\downarrow)), \tag{98}$$

or more economically,

$$2\int g_1(x)dx = \Sigma e_i^2 \Delta q_i, \tag{99}$$

where we have used the definition,

$$\Delta q_i = \int (q_i(\uparrow) + \overline{q}_i(\uparrow) - q_i(\downarrow) - \overline{q}_i(\downarrow))dx. \tag{100}$$

which gives the antiquark contribution explicitly. For the proton, in terms of the explicit quark types this gives us

$$2\int g_1^p(x)dx = \frac{4}{9}\Delta_u + \frac{1}{9}\Delta_d + \frac{1}{9}\Delta_s \tag{101}$$

with

$$2\int g_1^n(x)dx = \frac{1}{9}\Delta_u + \frac{4}{9}\Delta_d + \frac{1}{9}\Delta_s \tag{102}$$

for the neutron. We can now take the difference and obtain

$$2\int(g_1^p(x) - g_1^n(x))dx = \frac{1}{3}(\Delta_u - \Delta_d). \tag{103}$$

Now both Bjorken and Feynman recognised the relationship between this quark parton model expression and a static matrix element between nucleon states

$$\Delta_q \longleftrightarrow < p', s'|\overline{q}\gamma_\mu\gamma_5 q|p, s > \tag{104}$$

which appear in the $SU(3)_f$ description of weak decays. In particular,

$$\Delta_u - \Delta_d \longleftrightarrow < p', s'|\overline{u}\gamma_\mu\gamma_5 u - \overline{d}\gamma_\mu\gamma_5 d|p, s > = \frac{g_A}{g_V}. \tag{105}$$

That is to say we have arrived at a relationship with Nucleon Beta Decay! Explicitly we have

$$2\int(g_1^p(x) - g_1^n(x))dx = (\frac{1}{3})\frac{g_A}{g_V}, \tag{106}$$

which is known as the Bjorken Sum Rule [33].

Now is there anything we can say about g_1^p by itself? It is possible to work with the different $SU(3)_f$ operators, the currents I_0, I_3 and I_8 and ultimately the parameters F and D of $SU(3)$. These parameters are derived from the data on nucleon and hyperon beta decay, the weak interaction contributes the γ_5 to make contact with our spin operators. We do not have space here to treat this aspect as much more than a black box, a review of the subject is given by Gaillard and Sauvage [34]. It turns out that the terms which can be gleaned from the beta decay measurements are still not sufficient to determine g_1^p. One possible way to proceed was identified in 1974, one can assume that $\Delta_s = 0$, this leads to

$$\int g_1^p dx = \frac{g_A}{12}(1 + \frac{5}{3}\frac{(3F/D-1)}{(F/D+1)}, \tag{107}$$

$$\int g_1^n dx = \frac{g_A}{12}(-1 + \frac{5}{3}\frac{(3F/D-1)}{(F/D+1)}. \tag{108}$$

This is known as the Ellis-Jaffe Sum Rule [35].

4.3 Results of Polarized Lepton Scattering Experiments

So now we have some predictions for the theoretical side of the problem what is the situation with experiment. As usual, it is the fascination of the field, there are some complications. We have defined the measurable (theoretical) asymmetry by

$$\mathcal{A}_T = \frac{d\sigma(\uparrow\downarrow) - d\sigma(\uparrow\uparrow)}{d\sigma(\uparrow\downarrow) + d\sigma(\uparrow\uparrow)}. \tag{109}$$

However, the experimentally observable asymmetry is related to the theoretical asymmetry by the expression

$$\mathcal{A}_{exp} = P_B P_T f \mathcal{A}_T, \tag{110}$$

where P_B is the beam polarization, typically 0.8, P_T is the polarization of the free target nucleons, typically 0.8 and f is the fraction of nucleons in the target which are free and polarizable. The latter factor comes about because polarized targets are typically some complex molecule, ammonia or an alcohol, and not all the nucleons in such a target may be polarized. A typical value for f might be 0.15. Now when we multiply all these factors together, all are less than unity so we get a dilution of the theoretical asymmetry by a factor of approximately 0.06 to 0.1. That is to say that a theoretical maximal asymmetry, 100%, may result in an observable 6% effect. A large part of the experimental challenge lies in maximizing these dilution factors on the one hand, and then coping with the resulting small experimental effect on the others. Control of systematic effects is at a premium.

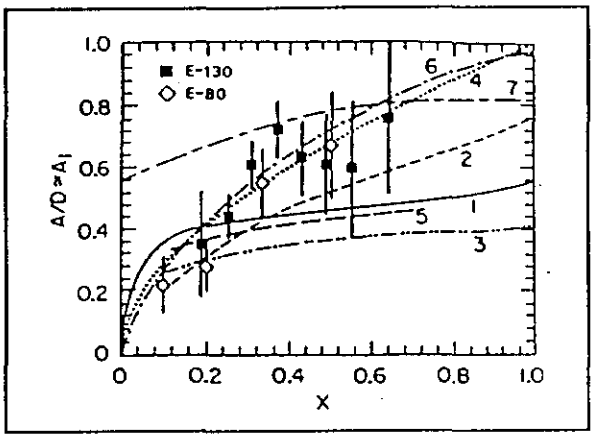

Figure 48: $\mathcal{A}_1$ as a function of x_{Bj} from the SLAC-Yale Experiment.

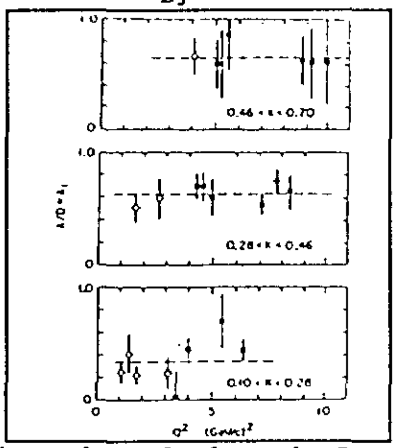
Figure 49: Q^2 dependence from the from the SLAC-Yale Experiment.

The first experiments to measure these effects were performed at SLAC in the seventies by a SLAC-Yale group [36]. Their results for $\mathcal{A}_1$ are shown in Fig. 48.

It is seen that the asymmetry for the proton is indeed non-zero and rises at high x_{Bj} to about 70−80%. Fig. 48 shows curves from a lot of models, we will not discuss each of these but merely comment that many of them envisage the asymmetry tending to unity as $x \to 1$ as the spin of the proton is imagined to reside on the single quark carrying all the proton momentum. Conversely, many models, for example, those based on Regge exchange envisage the asymmetry going to zero when the struck quark carries a small fraction of the proton momentum.

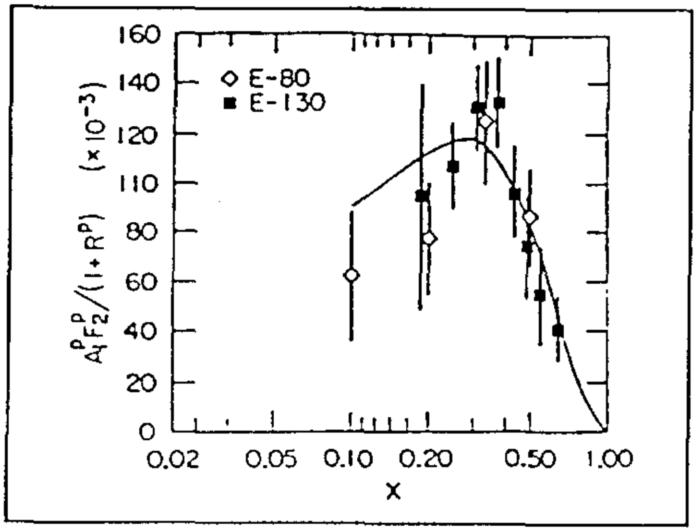

Figure 50: g_1^p as a function of x_{Bj} from the SLAC-Yale Experiment.

Figure 49 shows the Q^2 dependence of the SLAC-Yale data, within rather large errors there is no indication of a Q^2 dependence. This permits an averaging of the data and an attempt to construct g_1^p and compare with the Ellis-Jaffe Sum Rule. The data are shown in Fig. 50, the data themselves do not saturate the sum rule but with most reasonable extrapolations of the data to $x = 0$ there appeared to be no disagreement.

Recently an experiment has been performed using a muon beam at CERN [37]. The muon beam is naturally polarized due to the π decay mechanism by which it produced. Forward (backward) decay muons, dominantly of one helicity, carry large (small) fractions of the muon momentum in the laboratory and are therefore selected when the band of momentum of the muon beam is selected, see Fig. 51.

The polarized target used in the EMC experiment is shown in Fig. 52. In order to reduce systematic effects the target is divided in two, each half target is polarized in the opposite direction using slightly different radio frequencies to pump the polarization in the same magnetic field. This goes some way to reducing the systematic effects, however, the acceptance is slightly different from the two halves of the target leaving some residual corrections to be made. Further, the beam polarization is not easily reversible and for the target such an exercise took about 8 hours. These facts limited the number of reversals of the different polarizations which could be made. In most

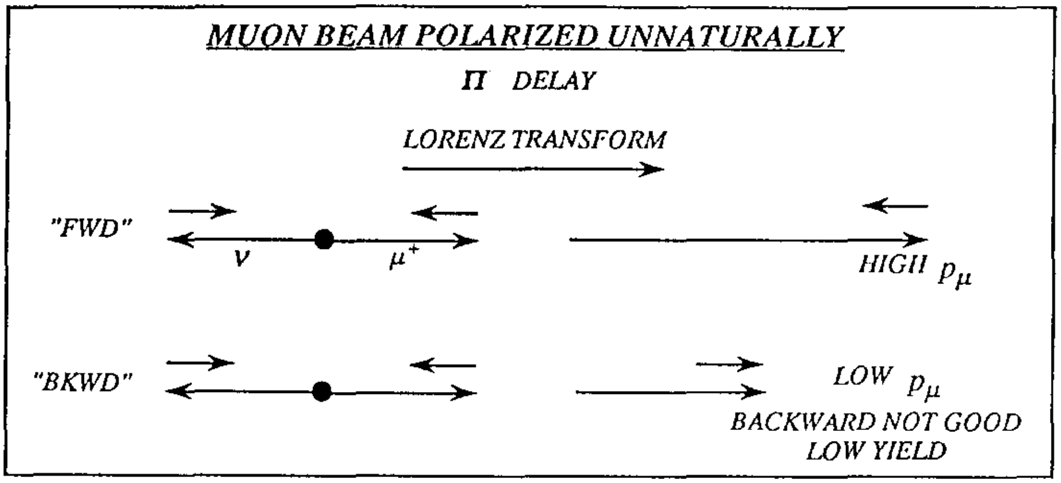

Figure 51: π decay in the centre of mass transforms to the laboratory frame giving a dependence of the muon helicity on its momentum.

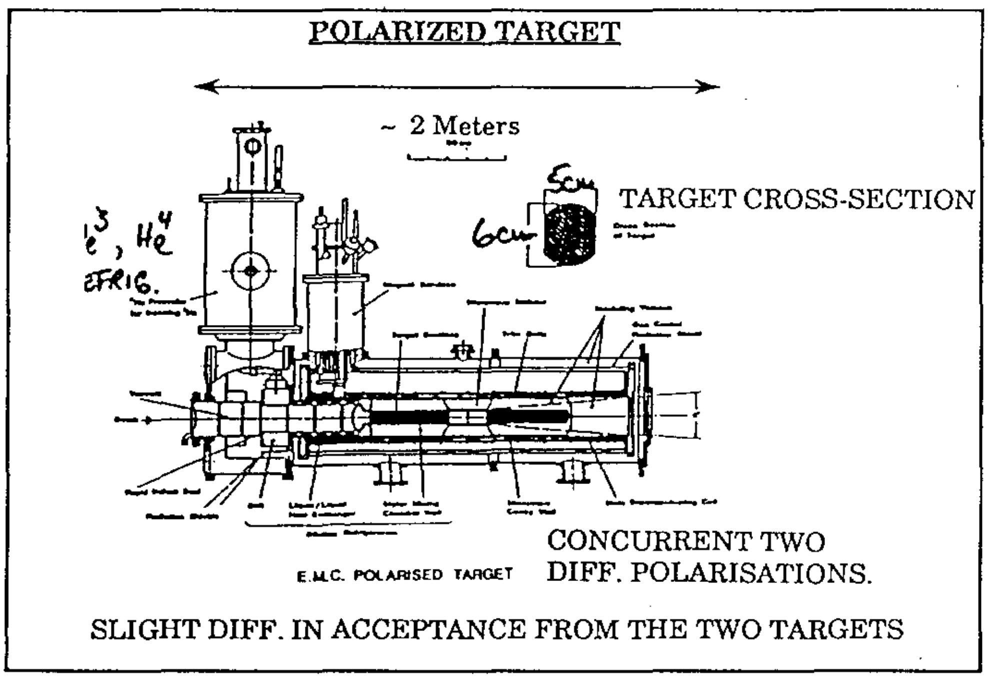

Figure 52: EMC Experiment Polarized Target.

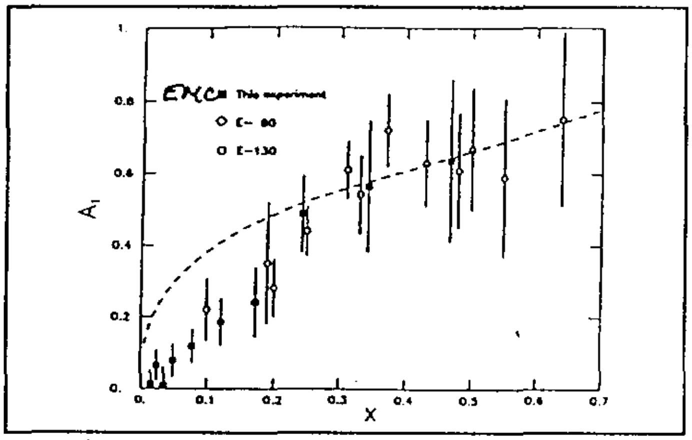

Figure 53: $\mathcal{A}_1$ as a function of x_{Bj} from the EMC Experiment.

polarization experiments, this is the technique by which systematic effects are limited or checked through measurement of false asymmetries.

The results of the measurement are shown in Fig. 53 and compared with the SLAC-Yale results. Where the kinematic ranges overlap there appears to be reasonable agreement. On the other hand, the new data appear to be below the typical model fit to the SLAC data. Again, converting to g_1^p, we obtain Fig. 54 which also contains the integral as a function of x_{Bj}. One can see that as $x_{Bj} \rightarrow 0$ the contribution to the integral decreases and it appears possible to extrapolate to $x_{Bj} = 0$. Also shown on the left-hand axis is the expectation from the Ellis-Jaffe Sum Rule and the data appear to be significantly below. This caused a fair degree of interest when the data were first presented. The Q^2 dependence of the data is shown for different x_{Bj} bins in Fig. 55, again within large errors it is flat.

So let us try to be a little more quantitative. The experiment measures $\mathcal{A}_1$ and

$$\int g(x)dx = \int \frac{\mathcal{A}_1(x)\mathcal{F}_2 dx}{2x}. \tag{111}$$

There is clearly some uncertainty in the extrapolation to low x, $\mathcal{F}_2$ is not well measured in that region and the sensitivity is enhanced by the $1/x$ factor. This was raised as an important flaw to the analysis but the consensus seems to be currently that there is no major problem in the procedure. So, in terms of numbers we have the prediction

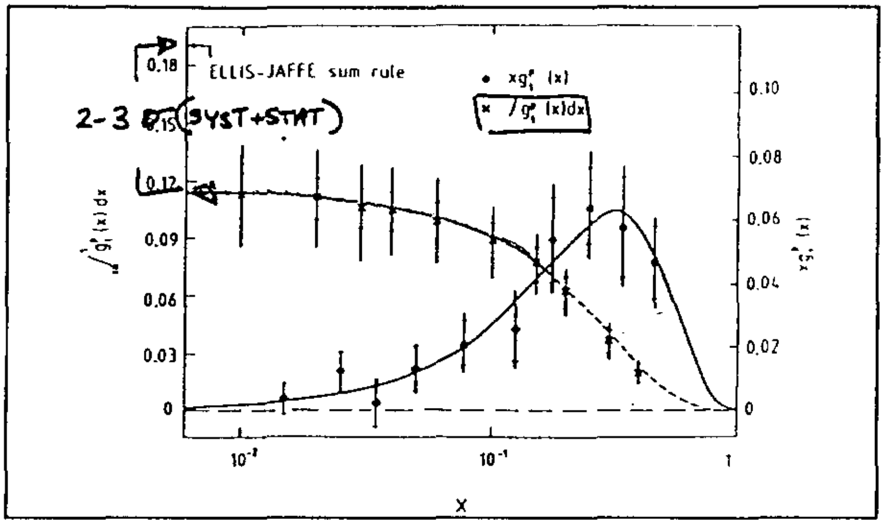

Figure 54: g_1^p as a function of x_{Bj} from the EMC Experiment.

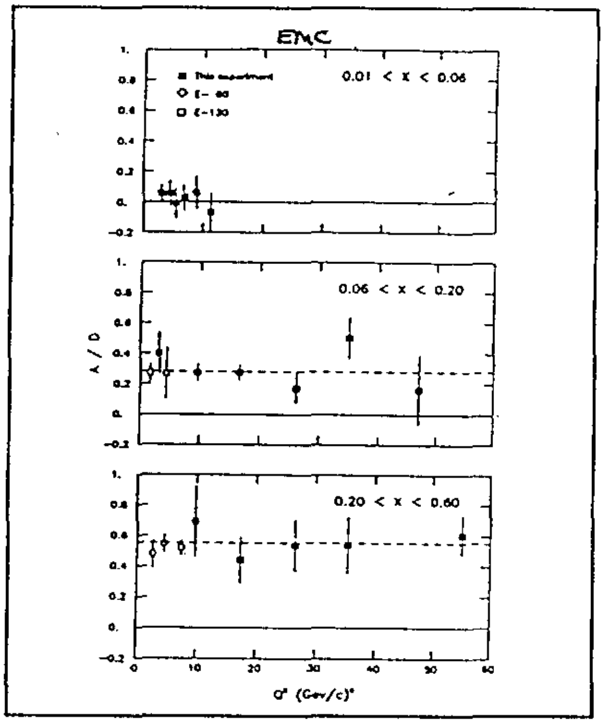

Figure 55: $\mathcal{A}_1$ as a function of Q^2 from the EMC Experiment.

$$\int_0^1 g_1^p dx = 0.189 \pm 0.005 \tag{112}$$

and the experimental result

$$\int_0^1 g_1^p dx = 0.114 \pm 0.012(stat) \pm 0.026(syst). \tag{113}$$

What are the implications? Using the assumption $\Delta_s = 0$ and the Bjorken Sum Rule, the experimenters [37] find

$$< S_z >_u = (1/2)\Delta_u = 0.348 \pm 0.023 \pm 0.051, \tag{114}$$

and

$$< S_z >_d = (1/2)\Delta_d = -0.248 \pm 0.023 \pm 0.051. \tag{115}$$

Putting these two together gives

$$< S_z >_q = 0.068 \pm 0.047 \pm 0.103. \tag{116}$$

This can then be provocatively restated as saying that only $(14 \pm 9 \pm 21)\%$ of the proton spin is carried by the quarks.

This interpretation of the result led to something of a furore, Close and Roberts emphasized the uncertainties in the extrapolation to $x = 0$, many people re-examined the analysis of the F/D ratios in hyperon beta decay and, especially, several people re-examined the possibilities if the strange quark contribution was not taken to be zero. Without that constraint the results become

$$< S_z >_u = 0.373 \pm 0.019 \pm 0.039, \tag{117}$$

$$< S_z >_d = -0.254 \pm 0.019 \pm 0.039, \tag{118}$$

$$< S_z >_s = -0.113 \pm 0.019 \pm 0.039, \tag{119}$$

and for the sum of quark contributions

$$< S_z >_{u+d+s} = 0.006 \pm 0.058 \pm 0.117. \tag{120}$$

This does not exactly solve the conundrum, however, some support for the experimental result comes from a neutrino elastic scattering experiment [38] analysis which is sensitive to similar matrix elements.

4.4 Conclusions on Polarization Effects

The implications of the data continue to be discussed, there is debate as to whether the intrinsically singlet $I_0 = \Delta_u + \Delta_d + \Delta_s$ is properly under control in the calculations and this leads also to discussions of the possible gluonic contribution. The latter is important because it could lead to experimental observables, for example, if the implication is really that the gluon contributes, still a theoretical argument, then the three jet events at low x in deep inelastic scattering from a polarized target should show a strong asymmetry. This was suggested by Mueller. It also leads to the possibility that single photon measurements using a polarized proton beam and a polarized target should show an asymmetry since they involve the gluon distribution.

There are several experiments proposed to repeat and extend the current results including measurements with the neutron which completes the components of the rigorous Bjorken Sum Rule. These and other possibilities were discussed in Breckenridge in 1989 [39].

4.5 Nuclear Effects; Introduction

Implicit in the quark parton model of deep inelastic scattering is the assumption that the photon interacts with the partons incoherently, there are no interference effects, there are no collective effects built into the formalism. The argument for this is that at large Q^2 any effects of binding on the scale of the mass of a hadron should have disappeared. Empirically also the weak Q^2 dependence characteristic of the parton model seemed to set in at rather low Q^2. Thus, many neutrino and muon experiments worked with targets of iron or marble or more exotic matter in order to maximize the luminosity of their measurements. The expectations for the effects of the internal motion of the nucleons in the nucleus, the Fermi motion, are illustrated in Fig. 56. Few experiments worked with more than one target except those looking for the hadronic? shadowing behaviour of the photon at very low Q^2.

The EMC experiment had taken data on hydrogen, deuterium, and iron targets. In 1981 it had presented hydrogen and iron measurements and also

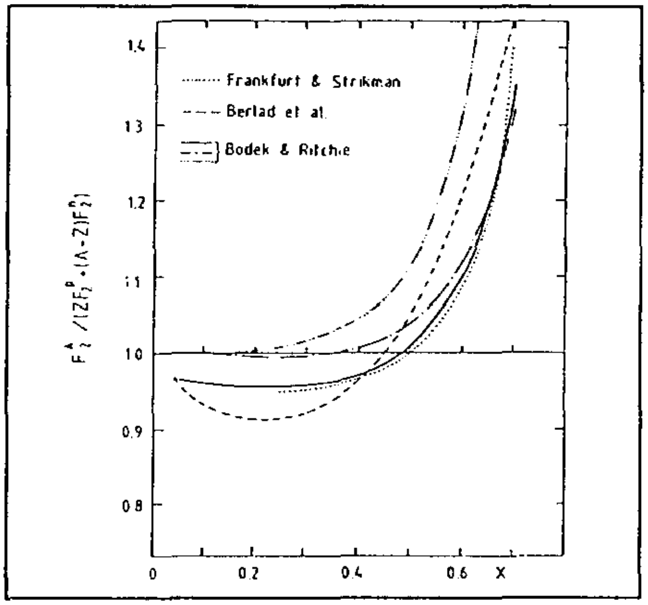

Figure 56: Expected Effects of Fermi Motion in a measurement of Iron compared to Deuterium.

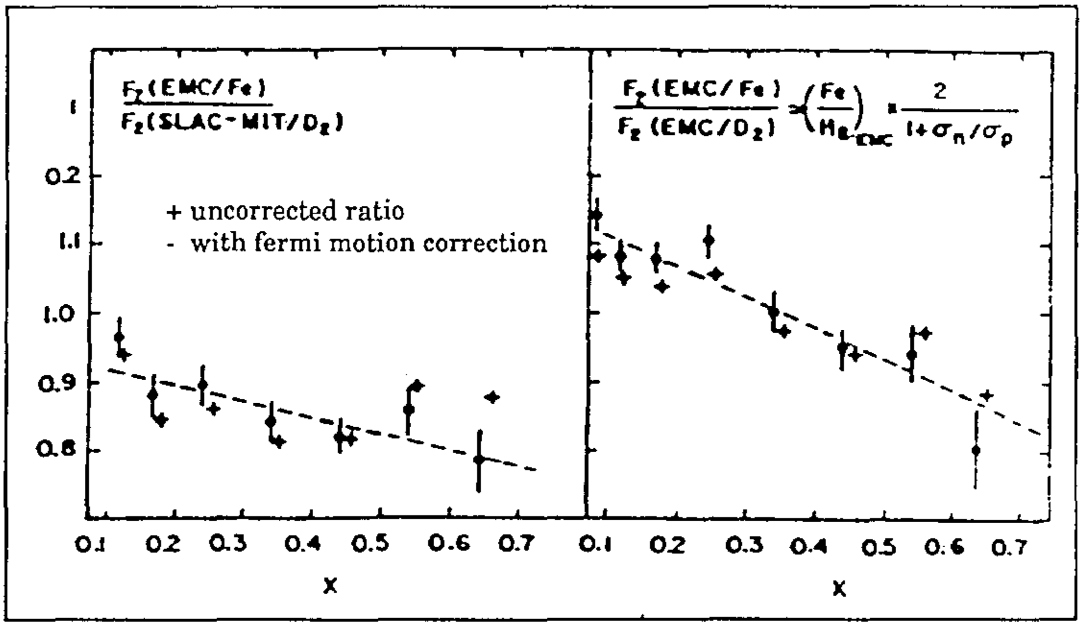

Figure 57: Ratios of Iron to Deuterium as constructed by Smadja.

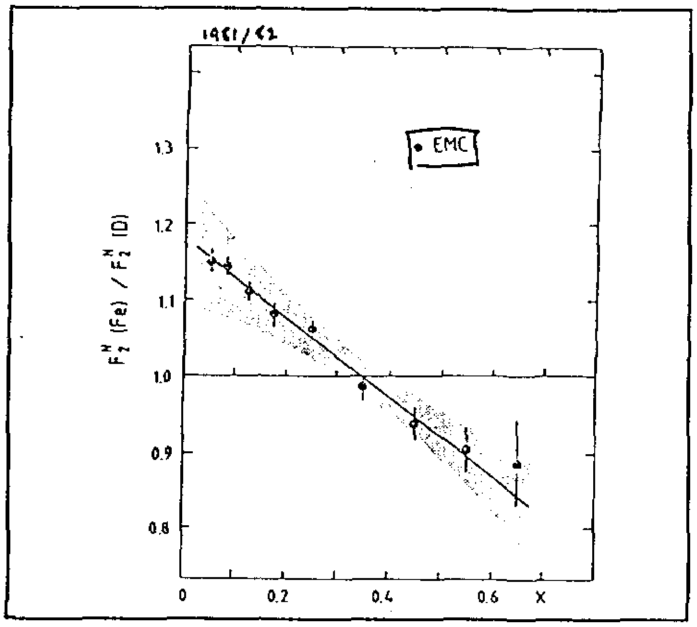

Figure 58: Ratio of Structure Functions of Iron and Deuterium [41] from the EMC experiment.

the neutron/proton ratio deduced from the deuterium measurements. At the Bonn conference, Smadja [40] reviewed deep inelastic structure functions and remarked that if he deduced an iron/deuterium ratio from the hydrogen and iron measurements and the n/p ratio using either EMC or SLAC data, as shown in Fig. 57, he did not obtain the value 1, but saw a dependence as a function of x_{Bj}. Within 18 months the EMC group published [41] the ratio of Deuterium to Iron as shown in Fig. 58. The shaded band indicated how the ratio could swing as a result of possible systematic errors in the experiment and in addition an overall $\pm 7\%$ relative normalization error was quoted.

This observation prompted a large number of theoretical ideas and more than 100 papers, only one of which is thought to predate the measurement. Because the understanding of the phenomenon has not completely been settled, I cannot give a pedagogic development of the theory as in previous sections. In what follows, I will merely intersperse some of the experimental data with some hint of a few of the theoretical ideas.

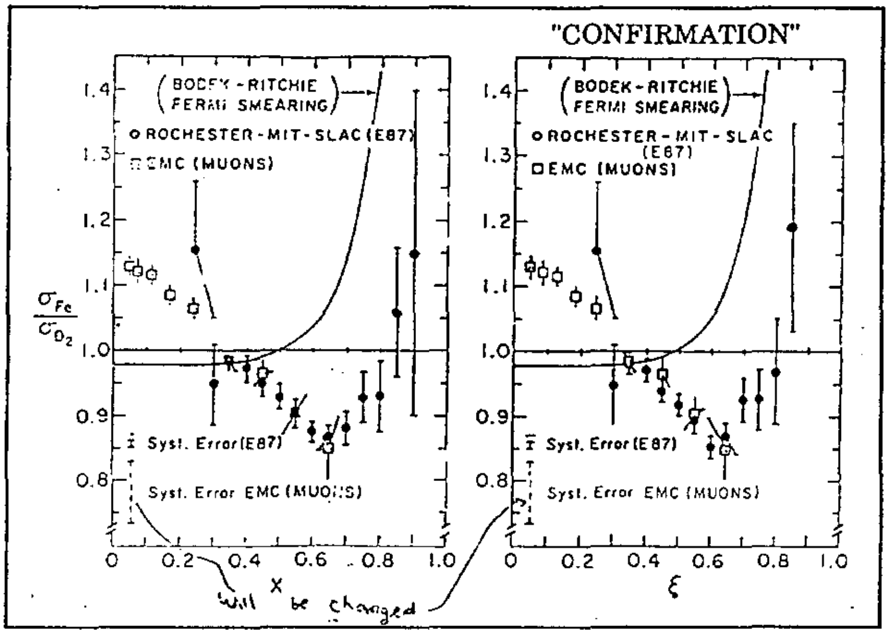

Figure 59: Ratio of Structure Functions of Iron and Deuterium [42] from the Rochester-MIT-SLAC experiment.

4.6 Nuclear Effects; Experimental Data and Theoretical Ideas

Following the first indication of an effect which followed the presentations at the Paris conference of 1983, a Rochester-SLAC group carried out a reanalysis of some of the early deep inelastic data from SLAC, using the dummy(empty) target flask data from a deuterium measurement they were able to confirm the gross features of the initial observation [42] as shown in Fig. 59.

Neutrino data do not really have sufficient statistics to make definitive statements. This is a pity since measurements with neutrinos should be able to distinguish whether the effect has its origins in a difference of the valence quark distributions or in the sea distributions. Another place where there is, in principle, a role for neutrino scattering is in examining deuterium itself. All measurements with muons or electrons assume that the deuteron is a simple sum of the proton and neutron and has none of the complications that appear to be present with higher A targets. Now, for neutrino scattering

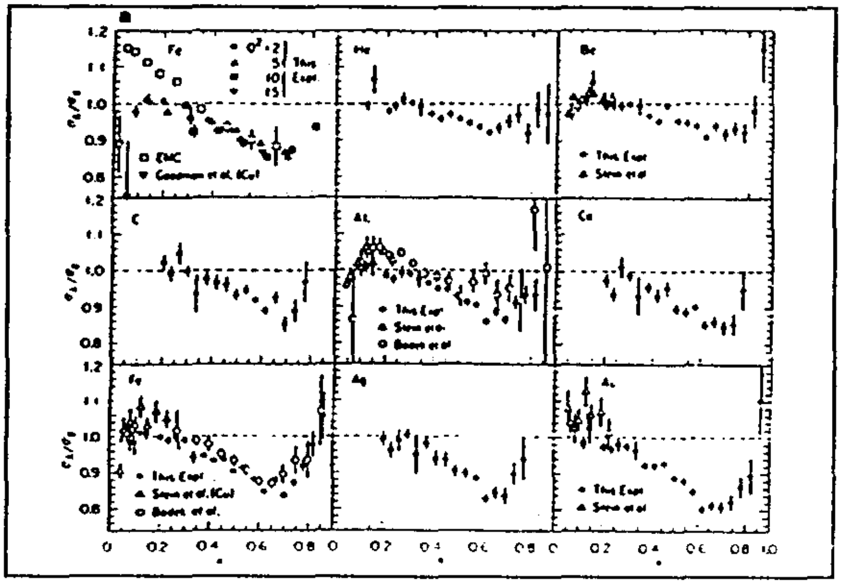

Figure 60: Results from the E139 Experiment at SLAC.

$$\nu p = \overline{\nu} n, \tag{121}$$

and hence,

$$\nu D = \nu p + \overline{\nu} n. \tag{122}$$

None of the neutrino experiments so far has had sufficient statistics on hydrogen and deuterium to check this relationship.

The new information is therefore dominated by charged lepton scattering. A series of dedicated experiments was performed to investigate systematically the behaviour of ratios of structure functions from a wide range of targets. Data from one of the first [43] is shown in Fig. 60. In these data it becomes clear that the ratio turns down below unity at very low x_{Bj} and turns up at very high x_{Bj}. The latter is expected from Fermi motion, the former is expected to happen to permit some smooth connection to the shadowing behaviour observed for real photons.

Now since the data from $E139$ are below unity, where the EMC data were above unity there was an apparent disagreement, although, at the limit of systematic errors. One possible difference between the two experiments is

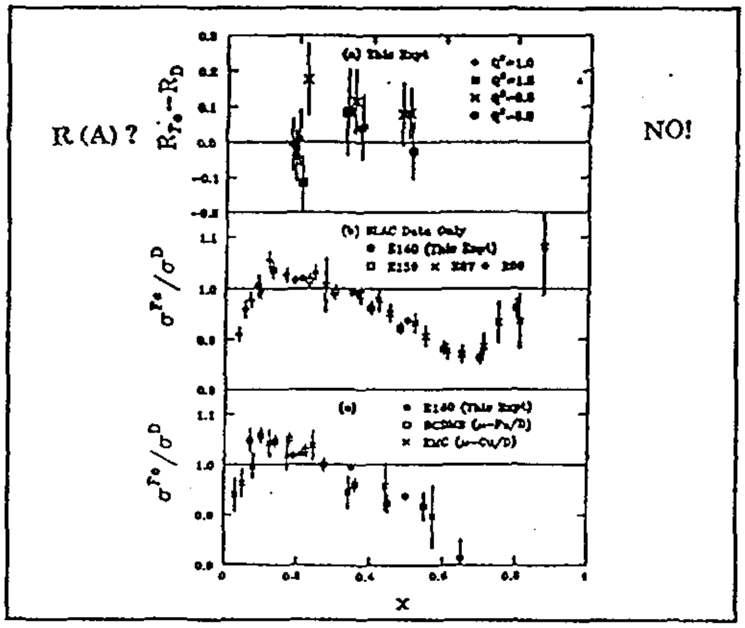

Figure 61: Results from the E140 Experiment at SLAC.

that the SLAC data could in principle be affected by a finite $R = \sigma_L/\sigma_L$ value if it varied with atomic number. The SLAC E140 Experiment [22] showed that this could not be the case by showing, Fig. 61, that R is independent, within errors, of the target.

Continuing the search for the origin of the effect EMC observed that the J/Ψ measurements from different targets were different and from their own data measured a ratio of 1.45 ± 0.21, a tentative 2σ effect between iron and deuterium. As we discussed in Lecture III, J/Ψ production can be related to the gluon distribution. This was not confirmed by the E691 photoproduction experiment [44] at Fermilab which measured the A dependence of J/Ψ production which they parameterized as A^{α} with the result $\alpha = 0.94 \pm 0.02 \pm 0.03$.

Meanwhile, the theoretical work continued apace. Here we will discuss two different approaches in an attempt to suggest that there may be a commonality to the different ideas.

One approach pursued by Close, Jaffe, Roberts and Ross in a series of papers [45] retains the quarks in the nucleons as the basic degrees of freedom but considers that the nucleon bags are modified in the nucleus such that the distributions of quarks are modified. They talk of a change of confinement scale in the nucleus. This "Dynamic rescaling" approach relates the ratio of structure functions $R_A(x) = \frac{2F_2^A}{AF_2^D}$ to the scale breaking derivative $\frac{d\ln F_2}{d\ln Q^2}(x)$. This leads them to the relationship

$$\frac{1}{A}F_2^A(x,Q^2) = F_2^N(x,\xi Q^2), \tag{123}$$

where ξ is the rescaling parameter. A comparison of the results of this model with the E139 data is shown in Fig. 62.

An alternative approach is epitomized by the work of Jaffe, Llewellyn-Smith, Thomas and recently Berger and Coester [46]. They remember that in conventional nuclear physics pions and higher isobars as well as nucleons are among the degrees of freedom used to describe the nucleus. They then consider the parton distributions in the nucleus as a convolution of the distributions of partons within these entities with the distribution of these entities within the nucleus.

$$\begin{aligned}\frac{1}{A}F_2^A(x,Q^2) = &\int_{z\geq x} dz f_N(z) {F_2}^N(x/z,Q^2) \\ &+ \int_{z\geq x} dz f_\pi(z) {F_2}^\pi(x/z,Q^2) \\ &+ \int_{z\leq x} dz f_B(z) {F_2}^B(x/z,Q^2)\end{aligned} \tag{124}$$

Momentum conservation and baryon number conservation lead to constraints on these distributions in much the same manner as we saw in the earlier sections. Figure 63 shows a comparison between one such fit to the data along with one of the rescaling comparisons.

Such a model leads to an enhanced anti-quark distribution in the higher A nuclei due to the pion which has an anti-quark as a valence quark.

4.7 Nuclear Effects; Concluding Remarks

As hinted at on several occasions in the previous section one of the interesting experimental unknowns at the moment is the ratio of anti-quark distributions as a function of A. The different models predict markedly different numbers. One way of measuring this quantity is to perform μ pair production experiments with a proton beam on different targets. Such an

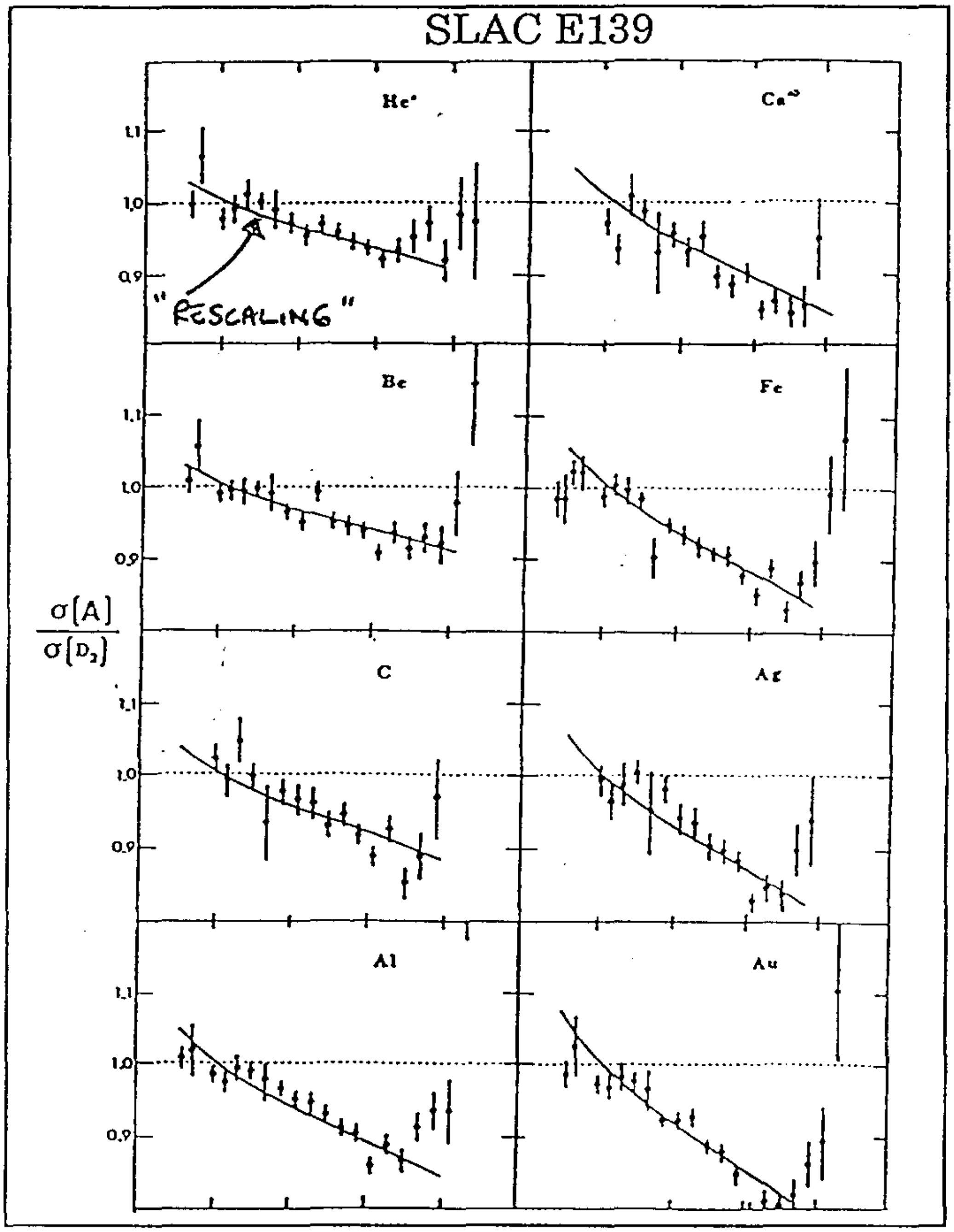

Figure 62: Comparison of the "Dynamic Rescaling Model" with the data.

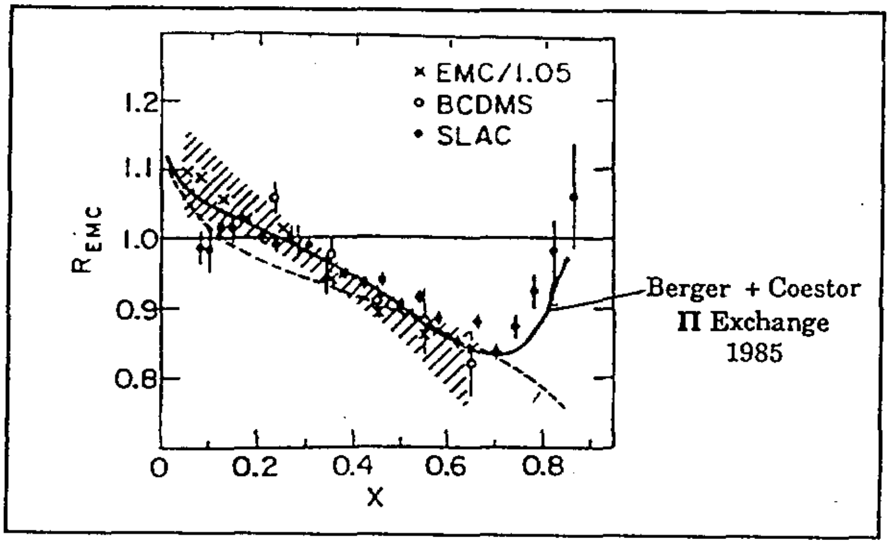

Figure 63: Comparison of the "conventional nuclear physics" model with the data.

experiment has been recently performed at Fermilab. The results, from E772 [47] were discussed by Chuck Brown in the following Lectures in this series.

Finally, some of the experiments on nuclear effects have started to concentrate on shadowing, low Q^2 and low x_{Bj}, effects. Among these is the muon scattering experiment at Fermilab E665. At the time of my Lectures results were not available. That is no longer true and it is with great pleasure that I include their measurements of the structure functions of Xenon and deuterium [48] extending down to very low x_{Bj} as the last data plot, Fig. 64, in the body of this document.

5 Conclusion

These conclusions are not going to be a summary of the Lectures, but a final attempt to extol the virtues of deep inelastic scattering. I do this by including, as Fig. 65, a copy from Panofsky's review talk at the Vienna Conference of 1968. At that time he had just finished including the first deep inelastic scattering measurements to be publically presented. At the time of

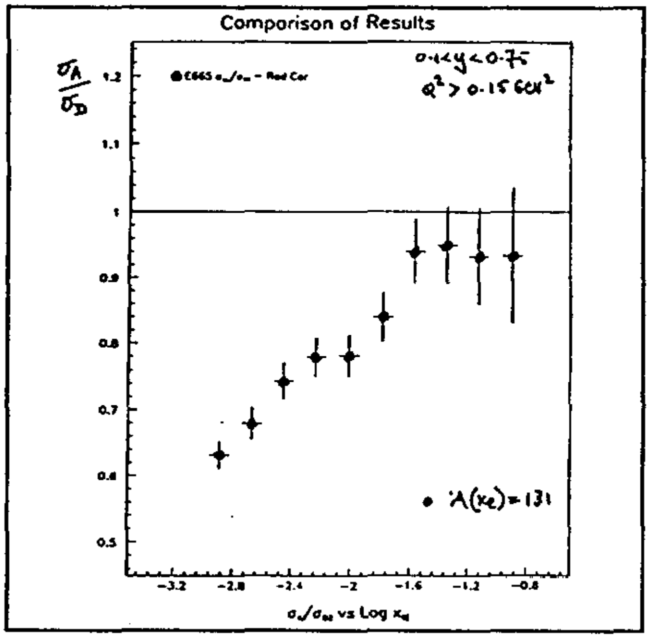

Figure 64: E665 Shadowing Measurements at Low x_{Bj}.

the Lectures those results were 21 years young, they had also outlived some of the other revolutionary activity of the world at that time.

6 Acknowledgements

I wish to thank Dan Green who, in not so subtle a manner, raised my feelings of guilt to such a level that I volunteered to give these Lectures. I also would like to take the opportunity to thank the ensemble of E665 colleagues and students who have contributed significantly to my enjoyment of physics over the last few years. The latter applies especially to Heidi Schellman who kindly read this document to try and find my gross errors. I would also like to thank Kristen Ford for her help in laying out this document.

PANOFSKY : RAPPORTEUR : VIENNA 1968.
(1 YEAR AFTER Bj's PREDICTION)

The qualitatively striking fact is that these cross-sections for inelastic electron and muon scattering leading to the continuum are very large and decrease much more slowly with momentum transfer than the elastic scattering cross-sections and the cross-sections of the specific resonant states; in fact, indications are that they probably decrease even more slowly than would be predicted from a simple ρ-vector dominance propagator. Therefore theoretical speculations are focused on the possibility that these data might give evidence on the behavior of point-like, charged structures within the nucleon.

TRUE: AT 21 IT IS STILL YOUNG.

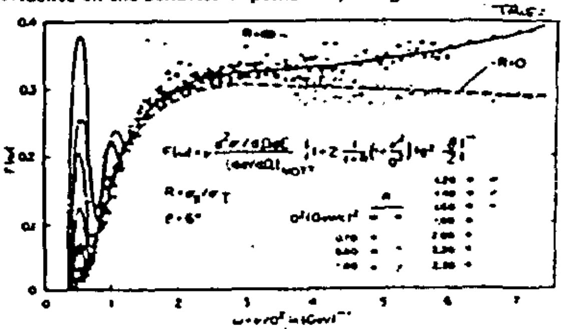

Plot of $F(\omega) = \nu W_2(q^2, \nu)$, as a function of $\omega = \nu / q^2$.

Figure 65: From Panofsky's Review Talk, Vienna, 1968.

7 Bibliography

- Halzen and Martin, Wiley, 1984.
- Quigg, Benjamin/Cummings, 1983.
- Drees and Montgomery Ann. Rev. Nucl. Sci. 33, 1983.
- Fisk and Sciulli Ann. Rev. Nucl. Sci. 32, 1982.
- Sloan, Smadja and Voss Phys. Rep. C, 182, 1988.

8 References

References

[1] H.E. Montgomery, R. Raitio (Ed.) and J. Linfors (Ed.), in *Gauge Theories of the Eighties*, Berlin: Springer-Verlag,1983.

[2] J. Friedman, and H. Kendall, *Ann. Rev. Nucl and Part. Sci.* **22**, 203 (1972).

[3] J.D. Bjorken, *Phys. Rev. Lett.* **16**, 408 (1966).

[4] W-K. Tung, *et al., Structure Functions and Parton Distributions, in Proceedings of the 1988 Summer Study on High Energy Physics in the 1990s*, World Scientific, 1990.

[5] EMC, O.C. Alkofer, *et al., Nucl. Instr. Meth.* **179**, 445 (1981);
EMC, J.P. Albanese, *et al., Nucl. Instr. Meth.* **212**, 111 (1983).

[6] BCDMS, D. Bollini, *et al., Nucl. Instr. Meth.* **204**, 333 (1983);
BCDMS, A. Benvenuti, *et al., Nucl. Instr. Meth.* **226**, 330 (1984).

[7] CDHS M. Holder, *et al., Nucl. Instr. and Methods* **148**, 235 (1978).

[8] D.B. Macfarlane, *et al., Z. Phys.* C**26**, 1 (1984).

[9] E665, M.R. Adams, *et al., Nucl. Instr. and Methods* **A291**, 533 (1990).

[10] S. Mishra, Issues in Neutrino Physics, Invited Review Talk, Physics at Fermilab in the 1990's, Breckenridge, Colorado, U.S.A, 1990.

[11] C. Guyot, *et al., A New Fixed Target Experiment for Precise Tests of QCD*, Saclay, March 14, 1989.

[12] K. Bazizi, *et al.,* High Luminosity Muon Scattering at Fermilab, Fermilab-Conf-90/39, 1990.

[13] M.J. Murtagh, R.J. Cence (Ed.) and A. Roberts (Ed.), 1981 Int. Conf. on Neutrino Physics and Astrophysics, Maui, Hawaii, I, 388.

[14] F. Sciulli, Proc. 1985 Int. Symp. on Lepton and Photon Interactions at High Energies, Kyoto, Aug. 1985.

[15] R. Voss, W. Bartel (Ed.) and R. Ruckl (Ed.), *Charged Lepton Interactions, Symposium on Lepton and Photon Interactions at High Energy*, Hamburg 1987, North Holland, Amsterdam, 1988.

[16] CDHS H. Abramowicz, *et al., Z. Phys.* c17, 283 (1983).

[17] CDHS H. Abramowicz, *et al., Z. Phys.* c15,19 (1982).

[18] Mark Oreglia, Munich 1988, Strange Sea Determination by Fermilab E744.

[19] BFP A.R. Clark, *et al., Phys. Rev. Lett.* **45**, 1465 (1980).
BFP G.R. Gollin, *et al., Phys. Rev.* **D24**, 55 (1981).

[20] EMC J.J. Aubert, *et al., Nucl. Phys.* **B213**, 1, 31 (1983).

[21] EMC J.J. Aubert, *et al., Nucl. Phys.* **B259**, 189 (1985); **B272**, 158 (1986); **B293**, 740 (1987).

[22] S. Dasu, *et al., Phys. Rev. Lett.* **61**, 1061 (1988).

[23] A.C. Benenuti, *et al., Phys. Lett.* **B237**, 592 (1990). See also J. Feltesse in Proc. 1989 Int. Symp. on Lepton and Photon Interactions at High Energy, Aug. 1989, Stanford, M. Riordan (Ed.).

[24] Altarelli, Parisi, *Nucl. Phys.* **B126**, 298 (1977).

[25] Chen, Zerwas, *Phys. Rev.* **D12**, 187 (1975).

[26] WA 70 M. Bonesini, *et al., Z. Phys.* **C38**, 371 (1988).

[27] UA6 A. Berasconi, *et al., Phys. Lett.* **B206**, 163 (1988).

[28] J. Huston, Taylor (Ed.) and Luth (Ed.), Rapporteur's talk at Int. Symp. on Lepton and Photon Interactions at High Energy, Stanford, August 1990.

[29] J.G. Morfin, and W-K. Tung, Fermilab-Pub-90/74,1990, submitted to *Z. Phys.* C.

[30] V.W. Hughes, and J. Kuti, *Ann. Rev. Nucl. and Part. Sci.*, **33**, 611 (1983).

[31] V. Papavassilliou, Ph.D. Thesis, Yale, 1987, Unpublished.

[32] J. Kuti, and V.F. Weisskopf, *Phys. Rev.* **D4**, 3418 (1971).

[33] J.D. Bjorken, *Phys. Rev.* **148**, 1467 (1966).

[34] J-M. Gaillard, T. Sauvage, *Ann. Rev. Nucl. Part. Sci.* **34**.

[35] J. Ellis, and R.L. Jaffe, *Phys. Rev.* **D9**,1444 (1974); **D10**, 1669 (E) (1974).

[36] M.J. Alguard, *et al., Phys. Rev. Lett.* **37**, 1261 (1976); **41**, 70 (1978). G. Baum, *et al., Phys. Rev. Lett.* **51**, 1135 (1983).

[37] J. Ashman, *et al., Phys. Lett.* **206B**, 364 (1988); J. Ashman, *et al., Nucl. Phys.* **B328**, 1 (1989).

[38] L.A. Ahrens, *et al., Phys. Rev.* **35**, 785 (1987).

[39] R. Brock, C.N. Brown, M.D. Corcoran, and H.E. Montgomery, Fermilab-Conf-90/37, 1990.

[40] G. Smadja, W. Pfeil (Ed.), Rapporteur's Talk, Int. Symp. on Lepton and Photon Interactions at High Energy, Bonn, 1981.

[41] EMC J.J. Aubert, *et al., Phys. Lett.* **123B**, 275 (1983).

[42] A. Bodek, *et al., Phys. Rev. Lett.* **50**, 1431 (1983); **51**, 534 (1983).

[43] R.G. Arnold, *et al., Phys. Rev. Lett.* **52**, 727 (1984).

[44] E691 M.D. Sokolof, *et al.*

[45] Close, Jaffe, Roberts and Ross.

[46] E. Berger, F. Coester, *Ann. Rev. Nucl. Part. Sci.* **37**, 463 (1987).

[47] D.M. Alde *et al., Phys. Rev. Lett.* **64**, 2479 (1990). S. Mishra, Fermilab Conf.-90/100-E (1990).

[48] M.R. Adams, *et al.,* Paper submitted to the 25th Int. Conf. on High Energy Physics, Singapore, Aug. 1990.